ELSEVIER

Contents lists available at ScienceDirect

### European Journal of Mechanics / B Fluids

journal homepage: www.elsevier.com/locate/ejmflu



# An Eulerian two-phase flow model investigation on scour onset and backfill of a 2D pipeline



Benjamin Tsai <sup>a,\*</sup>, Antoine Mathieu <sup>b</sup>, Eduard Puig Montellà <sup>b</sup>, Tian-Jian Hsu <sup>a</sup>, Iulien Chauchat <sup>b</sup>

- <sup>a</sup> Center for Applied Coastal Research, Civil and Environmental Engineering, University of Delaware, Newark, DE 19716, USA
- <sup>b</sup> Univ. Grenoble Alpes, CNRS, Grenoble INP, LEGI, 38000 Grenoble, France

#### ARTICLE INFO

Article history:
Available online xxxx

Keywords: Sediment transport Two-phase model Scour Piping Burial Backfill

#### ABSTRACT

The capability of an Eulerian two-phase model, SedFoam, in simulating the onset of scour underneath a pipeline and the backfill process is investigated. When a pipeline is slightly buried in the sediment bed, the scour onset can be caused by the piping process, which is due to seepage flow moving underneath the pipeline driven by the upstream-downstream pressure difference. To directly resolve piping as part of the scour simulation has been a challenge in the single-phase models. Alternatively, the two-phase models may be capable of simulating piping and backfill as it can resolve the interactions between the flow, structure, sediment transport, and seepage flow using a single set of governing equations and closures. To prove this point, SedFoam is validated by two laboratory experiments for the onset of scour underneath a pipeline. For piping driven by a prescribed upstream-downstream pressure difference, the model captures the temporal evolution of the pore-pressure gradient and the resulting fine-scale bathymetric change around the pipe consistent with the measured data. The model further provides insight into the seepage flow and the creeping movement of sediments during the onset of scour. When simulating piping driven by a unidirectional current, SedFoam successfully predicts piping driven by the upstream-downstream pressure gradient due to the incoming flow deceleration by the presence of pipeline and flow separation. As a proof-of-concept application, SedFoam is applied to simulate pipeline scour driven by an oscillatory flow. Although the boundary layer streaming effect is neglected, the model result shows realistic scour onset and the development of a scour hole. To demonstrate the model's capability to simulate the backfill process, the pipeline is then lowered artificially into the scour hole as an idealized treatment of the complex pipeline sinking process during scour. The resulting burial depth due to backfill is similar to that predicted by the empirical formula.

© 2021 Elsevier Masson SAS. All rights reserved.

#### 1. Introduction

Scour and burial of offshore and coastal structures, such as pipelines and foundations, and smaller objects, such as sea mines due to sediment transport driven by waves and currents can cause many maintenance and mitigation problems. Since the past decade, a great amount of research has been devoted to studying scour burial processes through laboratory experiments [1–6] and empirical parameterizations have been developed [7,8]. A recent work by Mattioli et al. [5] provide a comprehensive evaluation of several existing empirical formulas for scour around a surface-touching cylinder with their physical experiments. While some of the observed burial events may be caused by large-scale migration of sandbars, sandwaves and smaller bedforms [9,10], many

pipeline failures and burial of objects are caused by the local scour/burial processes.

Sumer and Fredsøe [11] provided a comprehensive literature review, including field surveys, on how pipeline scour can cause the sinking and its eventual burial. In general, the scour under a submarine pipeline is classified into three stages, the onset, the tunneling and the lee-wake erosion. The tunneling stage describes the rapid breaching and erosion processes between the pipeline and sediment bed after the scour onset. The leewake erosion signifies the subsequent erosion downstream of the scour hole dominated by vortex shedding in the wake of the pipeline [12]. As the presence of the pipeline itself can cause disturbance of the bottom boundary layer and local enhancement of bottom shear stress, scour holes underneath the pipelines can be initiated by the so-called piping mechanism [12,13]. Sumer et al. [1] reported a series of laboratory experiments investigating the onset of scour of 2D pipelines triggered by the piping processes. When a pipeline is slightly buried in the seabed, the onset

<sup>\*</sup> Corresponding author. E-mail address: btsai@udel.edu (B. Tsai).

of scour is due to pore water flow (seepage) passing underneath the pipeline caused by the pressure difference between upstream and downstream. In this case, it is the presence of pipeline and the resulting flow separation on either side of the pipeline establish a sufficient upstream-downstream pressure gradient and trigger the scour onset, while the bottom shear stress plays a minor role. By including seepage flow in the bed boundary condition of a Reynolds-averaged computational fluid dynamic (CFD) model, Li et al. [14] further provide quantitative evidences that the width of the equilibrium scour hole is proportional to the magnitude of upward seepage flow. Using measured laboratory data for the onset of pipeline scour driven by waves, Sumer et al. [1] also proposed the critical condition for the onset of scour using two nondimensional parameters, the embedment-to-pipediameter ratio e/D, and the Keulegan-Carpenter number, defined as  $KC = U_0T/D$ , where  $U_0$  is the wave orbital velocity amplitude and T is the wave period. For a comprehensive CFD simulation of scour, sinking, backfill and final burial processes, capturing the realistic scour onset is an important part of the integrated numerical simulation.

Mattioli et al. [15] use particle tracking velocimetry and demonstrate the importance of turbulent coherent structures during the scouring process around the pipeline. Due to tightly coupled fluid-particle and inter-particle interactions covering the full range of particle concentration, developing a high-fidelity model for scour burial processes is a challenging subject. When sediment concentration is low, usually some distance away from the bed, sediment transport is dominated by turbulence, while the turbulent eddies are also affected by the particles. In moderate to high concentration, transport is dominated by various types of intergranular interactions from intermittent collisions to long duration contacts. Through contributions from both particle inertia and interstitial fluid viscosity, various rheological closures are required [16-18]. In very high sediment concentration, sediment particles are nearly immobile and particle stresses serve as a critical role to model the fluid-like to solid-like transition and the overburden eventually is supported completely by the particle phase. In the meantime, fluid flow can pass through the pore space but experiences the drag force from granular skeleton. Due to these highly complex processes, conventional single-phase computational fluid dynamics (CFD) models for sediment transport split the transport into the suspended load and bedload regions. The suspended load transport can now be highly resolved to investigate the interaction between turbulent eddies and suspended sediments [19] and the characteristics of turbidity currents [20,21]. However, the bedload transport is often parameterized with empirical power law formula. While these conventional models had made progresses in predicting sediment transport, including bedform evolution and migration [22-24], and scour around a vertical pile [25], it is difficult to apply them to simulate scour onset due to piping because of the inherited assumption to treat transport layers of different concentration in an artificial manner.

Specifically, the single-phase models have been applied extensively to simulate pipeline scour in the tunneling and lee-wake erosion stages [26,27]. However, in these single-phase models, the submerged pipelines cannot be directly attached to or buried in the sand bed and a small gap has to be artificially introduced. Hence, these models cannot directly simulate realistic scour onset triggered by pore water flow (seepage) passing underneath the structure caused by the upstream-downstream pressure difference. What is needed is an explicit inclusion of a seabed module allowing the simulation of seepage flow within the existing CFD model for flow, turbulence and sediment transport [28]. Therefore, the modeling of realistic scour onset and subsequent scour development and burial processes is a highly complex problem.

A wide variety of industrial and geophysical flow applications, such as gas-liquid flows (e.g., [29-31]), fluidized bed (e.g., [32]), magma flows (e.g., [33]), and sediment transport, require descriptions based on the multiphase formulation. A significant progress has been made in the past several decades regarding the theoretical and numerical modeling approaches for multiphase systems. For sediment transport applications, the Euler-Lagrange formulation (e.g., [34]), Eulerian-Eulerian two-fluid formulation (e.g., [35-37]) and mixture formulation (e.g., [38]) have been successfully applied. A sediment transport model based on the multiphase formulation is able to resolve the full transport processes and allows seamless integration of turbulence, particlefluid, particle-particle interactions, and seabed dynamics [35,39]. Although the Euler-Lagrange approach is the most accurate in resolving the process of interest, the scour problem to be addressed in this study may involve at least several hundred millions of particles and hence it is not computationally feasible. Both the Eulerian two-fluid formulation and the mixture formulation can be applied to the present problem. The mixture approach is most computationally efficient, however, its closures on interaction between phases is more complex [40] and generally limited to particles of lower inertia. Therefore, we adopt the Eulerian two-fluid formulation in this study. SedFoam is an Eulerian twophase model for sediment transport applications developed in the open-source OpenFOAM modeling framework. SedFoam has been shown in the past several years to be capable of simulating current and wave-driven sheet flow transport [36,41-43]. SedFoam is built in the OpenFOAM framework and hence it is relatively easy to add other capabilities in the two-phase solver. For instance. SedFoam has been expanded for 3D large-eddy simulation capability to better resolve flow instabilities during flow reversal under waves in sheet flows [41]. SedFoam was also extended to resolve the air-water interface using the volume-of-fluid (VOF) type method in order to directly include surface wave processes in modeling sediment transport [42,43]. Recently, SedFoam has been extended to simulate scour below a submarine pipeline [44], 3D scour around a cylindrical pile [45], and wave-driven bedform evolutions [46].

Over the last decade, two-phase flow models have been applied to scour below the submarine pipeline to demonstrate the capabilities of the approach to reproduce different stages of the process. Using a  $k-\varepsilon$  model and a Bagnold rheology, Kazeminezhad et al. [47] were able to successfully reproduce the tunneling stage of scour under oscillatory flow conditions. Lee et al. [48] developed a  $k-\varepsilon$  model and the dense granular flow rheology  $\mu(I)$  [49] and successfully reproduced the tunneling stage of scour driven by a unidirectional flow. However, the model underpredict erosion during the lee-wake erosion stage. Ouda and Toorman [38] developed a mixture drift-flux model using a k- $\varepsilon$  closure and the dense granular flow rheology coupled with a VOF method to resolve the free surface waves. The authors successfully validated their model for the scour below pipelines under realistic free surface waves. The agreement with measured data regarding the erosion induced by the two intermittent largescale vortices was not satisfactory and this discrepancy has been attributed to the limitation of k- $\varepsilon$  turbulence closure in accurately resolving the vortices. More recently, Mathieu et al. [44] implemented a k- $\omega$  model and evaluated the different combination of turbulence model  $(k-\varepsilon \text{ or } k-\omega)$  and granular stress model  $(\mu(I)$ rheology or kinetic theory) for the scour below pipelines in unidirectional currents. While the granular stress models have little influence on the results, the turbulence model is demonstrated to be sensitive. Using a k- $\varepsilon$  model leads to better prediction of the scour depth during the tunneling stage but shows large discrepancies during the lee-wake erosion stage. On the contrary, using a  $k-\omega$  model, the scour depth is under-predicted during the tunneling stage but the model shows a good skill in the leewake erosion stage. This is due to the better prediction of vortex shedding with k- $\omega$  model compared to k- $\varepsilon$  model. It remains ongoing research to develop a robust two-equation closure in the Reynold-averaged two-phase models for simulating scour around structures. Moreover, existing two-phase models have not been applied to directly resolve scour onset via piping and backfill processes, even though the two-phase flow formulation seems to have all the essential modeling components.

The objective of this study is to demonstrate that a numerical model based on the two-phase flow formulation has the capability to model realistic scour onset due to piping and backfill. To test the minimum requirement of a two-phase model to simulate scour onset and backfill, we adopt an existing open-source two-phase model, SedFoam, and its model formulation is described in Section 2. In Section 3, we evaluate SedFoam's capability to simulate piping by comparing the results with two laboratory experiments reported by Sumer et al. [1]. In Section 4, we further apply SedFoam to simulate the pipeline scour driven by oscillatory flows with realistic onset (Section 4.1) and the backfill process (Section 4.2). Concluding remarks and future perspectives are given in Section 5.

#### 2. Model description

An open-source Eulerian two-phase model for sediment transport application, SedFoam is applied to simulate scour onset through piping. SedFoam [36,37] is a three-dimensional two-phase flow solver for sediment transport applications developed under the open-source CFD toolbox OpenFOAM. As discussed in [36,37], SedFoam solves the Eulerian-Eulerian two-phase equations derived by an ensemble-averaging operation over the local and instantaneous mass and momentum conservation equations of fluid and dispersed particles [50]. To avoid resolving 3D turbulence, turbulence-average (Reynolds average) can be further performed. In this study, we carry out two-dimensional numerical investigation by solving turbulence-averaged Eulerian two-phase equations. In the model, both the fluid and particle phases are solved through the governing equations of mass conservation which are written as

$$\frac{\partial \left(1-\phi\right)}{\partial t} + \frac{\partial \left(1-\phi\right)u_{i}^{f}}{\partial v_{i}} = 0 \tag{1}$$

for fluid phase and

$$\frac{\partial \phi}{\partial t} + \frac{\partial \phi u_i^s}{\partial x_i} = 0 \tag{2}$$

for sediment phase. In this study, the superscript f and s denote fluid and sediment phases and the subscript i=1,2 represents streamwise and vertical components respectively.  $\phi$  represents sediment volumetric concentration,  $u_i^f$  and  $u_i^s$  are the fluid and particle velocities. The momentum conservation of fluid phase can be written as

can be written as  $\frac{\partial \rho^{f} (1 - \phi) u_{i}^{f}}{\partial t} + \frac{\partial \rho^{f} (1 - \phi) u_{i}^{f} u_{j}^{f}}{\partial x_{j}}$   $= -\frac{\partial (1 - \phi) p^{f}}{\partial x_{i}} + \frac{\partial \tau_{ij}^{f}}{\partial x_{i}} + \rho^{f} (1 - \phi) g_{i} + (1 - \phi) f_{i} + M_{i}^{fs} \tag{3}$ 

and sediment phase momentum equation reads

$$\frac{\partial \rho^{s} \phi u_{i}^{s}}{\partial t} + \frac{\partial \rho^{s} \phi u_{i}^{s} u_{j}^{s}}{\partial x_{i}} = -\frac{\partial \phi p^{f}}{\partial x_{i}} - \frac{\partial p^{s}}{\partial x_{i}} + \frac{\partial \tau_{ij}^{s}}{\partial x_{i}} + \rho^{s} \phi g_{i} + \phi f_{i} + M_{i}^{sf}.$$
(4)

In these equations,  $\rho^f$  and  $\rho^s$  denote fluid and sediment density,  $p^f$  is fluid pressure,  $\tau_{ij}{}^f$  is the fluid phase stress, and  $p^s$  and  $\tau_{ij}{}^s$  are particle phase pressure and shear stress, respectively.  $g_i$  is the gravitation and is set to be  $-9.81 \, \text{m/s}^2$  (directed downward when

i=2) in this study. The external pressure gradient  $f_i$  can be used to drive the flow and it will be further explained in Section 4.1. The inter-phase momentum coupling term represents the drag force coupling the two phases which is written as:

$$M_i^{sf} = -M_i^{fs} = \phi K \left( u_i^f - u_i^s \right) - K \frac{v_t^f}{\sigma_c} \frac{\partial \phi}{\partial x_i}$$
 (5)

in which  $v_t^f$  is the turbulent viscosity,  $\sigma_c$  is the Schmidt number. For the drag parameter K, several options are available in SedFoam. Here, we adopt Ding and Gidaspow [32] formulation. Although this formulation was originally applied for fluidized bed, it has been validated with different benchmark cases of sediment transport [36,37,46]. The Ding and Gidaspow [32] formulation calculates the drag parameter according to high and low sediment concentration, which is written as:

$$K = \begin{cases} \frac{150\phi v^{f} \rho^{f}}{(1-\phi) d^{2}} + \frac{1.75\rho^{f} |u^{f} - u^{s}|}{d} &, \quad \phi \ge 0.2\\ \frac{0.75C_{d} \rho^{f} |u^{f} - u^{s}| (1-\phi)^{-2.65}}{d} &, \quad \phi < 0.2 \end{cases}$$
(6)

where  $v^f$  is the molecular viscosity of the fluid and  $C_d$  is the drag coefficient and it is calculated as

$$C_d = \begin{cases} \frac{24 \left(1 + 0.15 \text{Re}_p^{0.687}\right)}{\text{Re}_p} &, & \text{Re}_p \le 1000\\ 0.44 &, & \text{Re}_p > 1000 \end{cases}$$
 (7)

in which  $Re_p=(1-\phi)|u^f-u^s|d/\nu^f$  is the particle Reynolds number. The two terms on the right-hand side in Eq. (5) are due to drag force. The first term represents the drag induced by velocity difference between fluid and sediment phase. The second term results from the correlation between fluid turbulence and sediment concentration.

The fluid stress  $\tau_{ij}^f$  is calculated through the turbulent eddy viscosity  $\nu_l^f$ , written as

$$\tau_{ij}^f = \rho^f \left( 1 - \phi \right) \left[ 2 \left( \nu_t^f + \nu^f \right) S_{ij}^f - \frac{2}{3} k \delta_{ij} \right] \tag{8}$$

where  $S_{ij}^f = 1/2 \left( \partial u_i^f / \partial x_j + \partial u_j^f / \partial x_i \right) - 1/3 \left( \partial u_k^f / \partial x_k \right) \delta_{ij}$  is the deviatoric strain rate tensor of the fluid phase. To solve turbulent eddy viscosity  $v_t^f$ , the Wilcox (2006) k- $\omega$  model [51] is used in this study and it is written as

$$v_t^f = \frac{k}{\max\left[\omega, C_{\lim} \frac{\left\| S_{ij}^f \right\|}{\sqrt{C_{\mu}}}\right]} \tag{9}$$

where  $C_{\text{lim}}$  is a stress limiter coefficient (see Table 1), k is the turbulent kinetic energy and  $\omega$  is the specific turbulent energy dissipation rate. These two turbulence quantities are calculated by their balance equations:

$$\frac{\partial k}{\partial t} + u_j^f \frac{\partial k}{\partial x_j} = \frac{R_{ij}^f}{\rho^f} \frac{\partial u_i^f}{\partial x_j} + \frac{\partial}{\partial x_j} \left[ \left( v^f + \frac{v_t^f}{\sigma_k} \right) \frac{\partial k}{\partial x_j} \right] 
- C_\mu \omega k - \frac{2K \left( 1 - t_{mf} \right) \phi k}{\rho^f} - \frac{1}{1 - \phi} \frac{v_t^f}{\sigma_c} \frac{\partial \phi}{\partial x_j} \left( \frac{\rho^s}{\rho^f} - 1 \right) g_j$$
(10)

and 
$$\begin{split} &\frac{\partial \omega}{\partial t} + u_j^f \frac{\partial \omega}{\partial x_j} = C_{1\omega} \frac{\omega}{k} R_{ij}^f \frac{\partial u_i^f}{\partial x_j} + \frac{\partial}{\partial x_j} \left[ \left( v^f + \frac{v_t^f}{\sigma_\omega} \right) \frac{\partial \omega}{\partial x_j} \right] - C_{2\omega} \omega^2 \\ &- C_{3\omega} \frac{2K \left( 1 - t_{mf} \right) \phi \omega}{\rho^f} - \frac{C_{4\omega}}{1 - \phi} \frac{\omega}{k} \frac{v_t^f}{\sigma_c} \frac{\partial \phi}{\partial x_j} \left( \frac{\rho^s}{\rho^f} - 1 \right) g_j \\ &+ \sigma_d \frac{1}{\omega} \frac{\partial k}{\partial x_j} \frac{\partial \omega}{\partial x_j} \end{split}$$

**Table 1** Empirical coefficients for the k- $\omega$  turbulence model.

$\sigma_k$	$\sigma_{\omega}$	$C_{\mu}$	$C_{1\omega}$	C <sub>2ω</sub>	$C_{3\omega}$	$C_{4\omega}$	C <sub>lim</sub>
0.6	0.5	0.09	0.52	0.0708	0.35	1	0.875

where  $R_{ij}^f = \rho^f (1-\phi) \left(2 v_t^f S_{ij}^f - 2/3 k \delta_{ij}\right)$  is the Reynolds stress. The fourth terms on the right-hand-side of the two equations take into account sediment damping effect due to particle inertia. The parameter  $t_{mf}$  is to characterize the degree of correlation between particles and fluid velocity fluctuations which is modeled as  $t_{mf} = e^{-B \cdot \text{St}}$ , in which B is an empirical coefficient (B = 0.25 in this study) and St is the Stokes number. More details can be found in [36] and [37].  $\sigma_k$ ,  $\sigma_\omega$ ,  $C_\mu$ ,  $C_{1\omega}$ ,  $C_{2\omega}$ ,  $C_{3\omega}$ ,  $C_{4\omega}$  are model coefficients that are defined in Table 1 and  $\sigma_d$  is the coefficient for the cross-diffusion term which is given by:

$$\sigma_{d} = \begin{cases} 0 & , & \frac{\partial k}{\partial x_{j}} \frac{\partial \omega}{\partial x_{j}} < 0\\ 1/8 & , & \frac{\partial k}{\partial x_{i}} \frac{\partial \omega}{\partial x_{j}} \ge 0 \end{cases}$$

$$(12)$$

The closure of particle phase stress is the most essential component in modeling sediment transport in high sediment concentration. In SedFoam, different physics contributing particle stress are modeled according to sediment concentration. In lower concentration, short-lived particle collision and interaction between particles and turbulent eddies are the source of particle stress and it is modeled via turbulent viscosity and a kinetic component of particle stress as part of the kinetic theory of granular flow. Turbulent suspension (see Eq. (5)) and particle stress in this lower sediment concentration range (volume concentration around 5-10%) plays an important role in suspending sediment and serves as a transition to dilute concentration (<5%) where suspension is fully taken over by vortices and turbulence. In moderate to high concentration, particle stress is dictated by shear-induced intergranular interaction and it is modeled by the  $\mu(I)$  rheology in this study. Particle shear stress in this intermediate concentration range serves a vital role for the exchange of flow momentum between water phase and sediment. Meanwhile, the vertical gradient of particle pressure becomes the major suspension mechanism of sediment as turbulence is diminished close to the bed. Near-bed load transport occurs in this concentration range is key to scour and burial process. In very high concentration when sediment particles are nearly immobile, particle stresses serve a critical role to model the transition of fluid-like (plastic behavior) to solid-like (elastic) behavior and the overburden eventually is supported completely by particle phase. The closure of particle stresses in this high concentration region of enduring contact is modeled empirically following the expected elastic behavior in the soil mechanics.

In SedFoam, particle phase pressure and shear stress are modeled by a collisional component (super-script 'sc') in the low to intermediate concentration regime, and a frictional component (super-script 'sf') for high concentration regime of enduring contact.

$$p^s = p^{sc} + p^{sf} \tag{13}$$

$$\tau_{ij}^s = \tau_{ij}^{sc} + \tau_{ij}^{sf} \tag{14}$$

Two different inter-granular stress models are available: the kinetic theory of granular flow and the dense granular flow rheology  $\mu(I)$ . The kinetic theory of granular flow models particle stress and particle pressure by the granular temperature and more details can be found elsewhere [36,37]. In this study, we

adopt dense granular flow rheology, which is developed based on dimensional analysis and empirical data to model granular flow with a liquid-like behavior [49,52]. The shear stress  $\tau_{ij}^s$  is calculated by

$$\tau_{ij}^{s} = \mu (I) p^{s} \frac{S_{ij}^{s}}{\sqrt{2S_{ij}^{s} \cdot S_{ij}^{s} + D_{\text{small}}^{2}}}$$
 (15)

where  $S_{ij}{}^s$  is the shear strain rate tensor of the sediment part,  $D_{\rm small}$  is a very small nominal strain rate (s<sup>-1</sup>), which serves as regularization parameter to avoid the denominator being zero in highly concentrated sediment bed (the rate of strain of sediment phase velocity eventually becomes zero in the immobile bed), which causes numerical instability or very small time steps. It is chosen to be  $10^{-4}$  s<sup>-1</sup> in this study following previous works, [53] and [44].  $\mu(I)$  can be calculated through

$$\mu(I) = \mu_s + \frac{\mu_2 - \mu_s}{I_0/I + 1} \tag{16}$$

where  $\mu_s$ ,  $\mu_2$ ,  $I_0$  are model coefficients with the values of 0.63, 1.13, 0.6 and  $I = d\sqrt{\rho^s/p^s}\sqrt{S^s_{ij} \cdot S^s_{ij}}$  is the inertial number (d is the particle size). An empirical formula for the frictional component of particle pressure  $p^{sf}$  is provided by Johnson and Jackson [54] which is written as

$$p^{sf} = \begin{cases} 0, & \phi < \phi_f \\ F \frac{\left(\phi - \phi_f\right)^m}{\left(\phi_{\text{max}} - \phi\right)^n}, & \phi \ge \phi_f \end{cases}$$

$$(17)$$

in which F, m, n,  $\phi_f$ ,  $\phi_{\rm max}$  are model coefficients and the values are 0.05, 3, 5, 0.45 and 0.625. In  $\mu(I)$  rheology model, the shear-induced pressure can be obtained from the dilatancy law  $\phi(I) = \phi_{\rm max}/(1+B_\phi I)$  proposed by Boyer et al. [17]. This gives the following shear induced pressure [55]

$$p^{sc} = \left(\frac{B_{\phi}\phi}{\phi_{\text{max}} - \phi}\right)^2 \rho^s d^2 \left\|S_{ij}^s\right\|^2 \tag{18}$$

The well-known ill-posedness of the equations (e.g., [40,50]) is remediated due to the fluid and particle phase stresses and more detailed model formulation.

#### 3. Scour onset by piping

In this section, SedFoam is validated by two laboratory experiments for the onset of scour underneath a pipeline reported by Sumer et al. [1]. In the first experiment, scour onset is simply driven by a prescribed upstream-downstream pressure difference (Section 3.1) in order to understand how seepage flow drives seabed response and breaching and their relationship with the prescribed pressure difference. In Section 3.2, the upstreamdownstream pressure difference is caused by the presence of a pipeline interrupting the passage of a current. In this case, we evaluate the model capabilities in both simulating turbulent flow and flow separation around the pipeline and their effects on the seepage flow and piping. The initial conditions and model parameters are set to match the values reported in the experiment. No compaction of the initial sediment bed is reported in the experiment. Second order schemes (Gauss linearUpwind) and the preconditioned bi-conjugate gradient (PBiCG) pressure solver are used in this paper for all simulations.

## 3.1. Piping driven by a prescribed upstream-downstream pressure difference

Piping is the onset of scour caused by the seepage flow passing underneath a structure, such as a pipeline, driven by the upstream

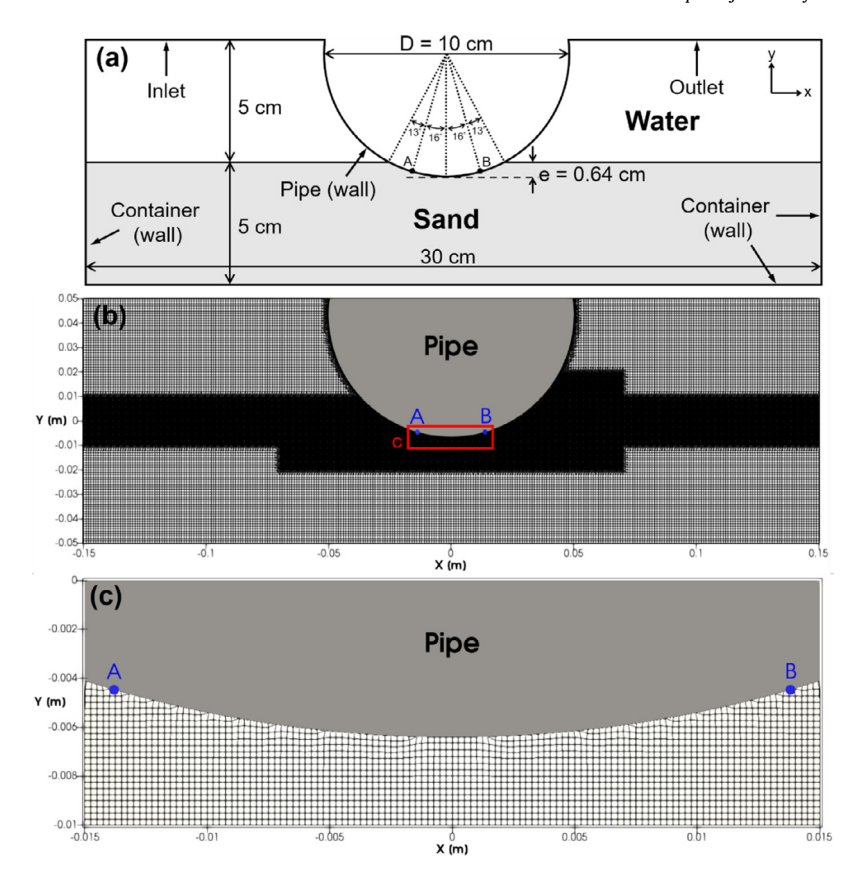


Fig. 1. (a) The sketch of the domain setup of the static onset case, (b) the wide view of the mesh, and (c) the enlarged view of the mesh near the bottom. Two blue points, A and B, represent the locations of the numerical fluid pressure probes.

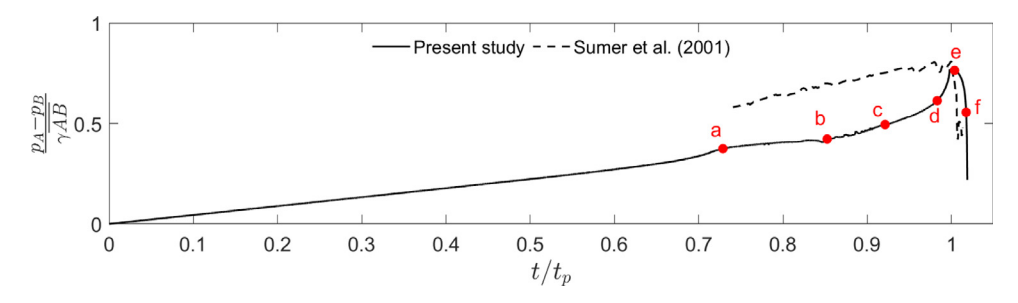
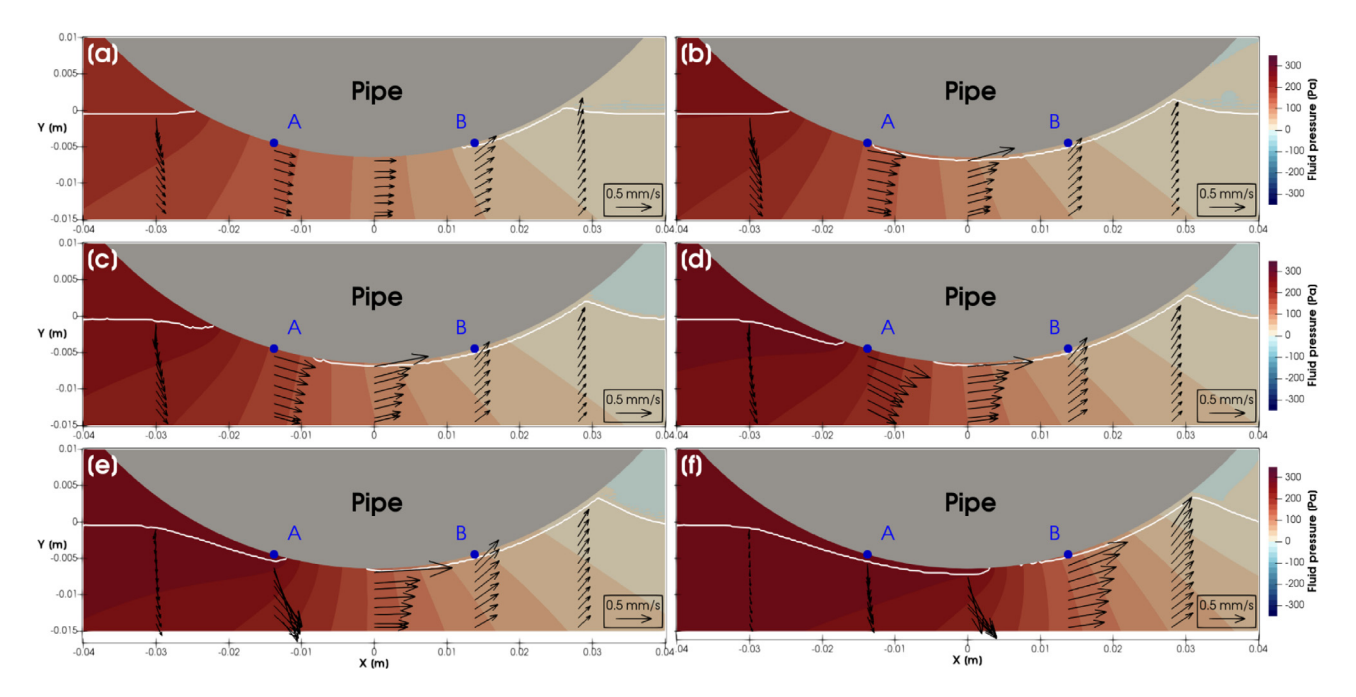


Fig. 2. The time series of the fluid pressure gradient between probe A and B under prescribed pressure difference between the model result (black solid line), experimental data of Sumer et al. [1] (black dash line). Red dots signified by a-f are selected instants to be discussed in Fig. 3.

and downstream pressure difference. In reality, the upstreamdownstream pressure difference can be caused by a variety of fluid dynamic processes, such as flow separation and they will be addressed later. As a first step, we significantly simplify the fluid dynamic effect by carrying out a 2D piping simulation driven by a prescribed pressure difference similar to the laboratory experiment reported by Sumer et al. [1]. As presented in Fig. 1(a), the domain size is established as 30 cm in the horizontal (x)direction and 10 cm in the vertical (y) direction with the initial sediment bed specified to cover the lower 5 cm of the domain. The sediment bed consists of sand with grain diameter d = 0.18mm and specific gravity s = 2.65. The circular pipe has a diameter of D = 10 cm located at the center of the domain. Hence, we define x = 0 as in the middle of the pipe and y = 0 located at the initial bed surface. Following the physical experiment, the pipe is initially buried at a small burial depth of e = 0.64 cm (see Fig. 1(a)) and hence the embedment-to-pipe-diameter ratio is e/D = 0.064. The upper left boundary is specified as an inlet and the fluid pressure is gradually increased to simulate a rising water

level. The fluid pressure on the upper right boundary, modeled as an outlet, is specified to be zero to mimic a constant water level. The left, bottom, right boundaries of the domain and the pipe surface are set to be the wall boundaries. Two pressure transducers were installed during the Sumer et al. [1] experiment. Following the experimental setup, two numerical probes, A and B with a distance of  $\overline{AB} = 2.8$  cm, are set to record the time series of the total pressure of fluid (or the piezometric head), and they will later be used to compare with the measured data.

As shown in Fig. 1(b) and (c), the 2D mesh is first constructed with uniform grids of 1 mm by 1 mm squares and then further refined into 0.25 mm by 0.25 mm fine grid near the bed surface and the pipe using an OpenFOAM built-in tool, snappyHexMesh. The total number of grid points used in this simulation is approximately 131 thousand. A grid convergence test is carried out to justify the fine grid size of 0.25 mm used near the pipe. In the laboratory experiment carried out by Sumer et al. [1], the entire time series of upstream–downstream pressure difference was not reported. However, it is clear that the pressure difference



**Fig. 3.** Sequence of piping process with fluid pressure (contour), sediment bed (white line, denotes the contour of sediment concentration equals  $\phi_f$ ) and seepage velocity (black arrows) correspond to (a)  $t/t_p = 0.73$ , (b)  $t/t_p = 0.85$ , (c)  $t/t_p = 0.92$ , (d)  $t/t_p = 0.98$ , (e)  $t/t_p = 1.00$  and (f)  $t/t_p = 1.02$ . Time steps correspond to the red dots in Fig. 2.

was increased very slowly such that the final piping occurred at about 1100 s since the start of the experiment. To save computational time in the present simulation, we speed up the increase of pressure difference so that piping occurs at only half of the time compared with the experiment. For this reason, the model-data comparison is presented here using normalized time. The simulation was carried out using 36 computing cores and it took about 29 h (1044 CPU hours) for the entire 750-second run.

The modeled fluid pressure gradient (piezometric head gradient) between probes A and B are shown in Fig. 2. Since the increase rate of the fluid pressure in Sumer et al. [1] is not clearly stated, we use the peak time  $t_p$ , which is defined as the time when reaching the peak pressure gradient, to scale the time series between the measured and modeled time series. The fluid pressure gradient is calculated through the fluid pressure difference between probe A and B divided by the specific weight of the water  $\gamma$  and the distance AB between the two probes. Our simulation result shows a good agreement with the measure critical fluid pressure gradient (error within 5%) right before the breakthrough (see point e in Fig. 2) and the rapid decay of pressure gradient after the breakthrough. However, the pressure gradient approaching breakthrough is lower than the measured data (see point a, b, c, d). Although model results show a linear increment of pressure gradient similar to the measured value sometime before the breakthrough (albeit at a lower value, see point a, b, c), shortly (about 0.03  $t_p$ ) before the breakthrough occurs, the modeled pressure gradient increases nonlinearly while measured data still shows a more or less linear increase. The discrepancy can be caused by the uncertainties of the initial sediment bed preparation (small difference in the initial concentration or small air content) in the physical experiment or the faster fluid pressure increase rate in the simulation. It is also possible that the present model lacks a good sub-model for soil dilatancy effect, and this point will be discussed later. Nevertheless, our simulation captures the essential pore pressure gradient evolution during piping.

More insights into the piping process and their similarities with those reported in Sumer et al. [1] can be gained by examining the spatial distribution of fluid pressure and the seepage

velocity at different moments in time (see Fig. 3). Although the pipe is initially buried, the bed on either side of the pipe is completely flat. At  $t/t_p = 0.73$  (see Fig. 3(a)), a small seepage velocity of about 0.3 mm/s is observed in the sand bed below the pipe. Meanwhile, a small gap at the downstream side between the pipe and sediment bed starts to develop, and a barely notable rise of sand can be seen. In Fig. 3(b), this gap grows from probe B and extends to probe A and the seepage velocity near the gap has increased to 0.5-0.7 mm/s. As the gap is growing, the sediment bed at the downstream side rises more significantly. Once the gap reaches probe A, it starts to retreat toward the downstream side (see Fig. 3(c)). Meanwhile, the sediment bed on the upstream side starts to be pushed toward the downstream side (Fig. 3(c) and (d)) while the peak seepage velocity increase to about 1 mm/s. Meanwhile, a larger gap at the front of the pipe can be clearly seen and the pressure gradient starts to increase sharply (see point d in Figs. 2 and 3(d)) until reaching the maximum value (see point e in Fig. 2), which is the time when the upstream bed pushback reaches probe A as shown in Fig. 3(e). At this moment, the seepage velocity also shows a significant vertical (downward) component just under probe A, suggesting that the sediment mobility locally becomes higher. After reaching the maximum pressure gradient, the fluid pressure gradient dramatically decreases while the gap at the front of the pipe rapidly extends to the downstream (Fig. 3(f), and point f in Fig. 2) where the sediment bed has risen to about half a millimeter and seepage velocity also reaches beyond 1 mm/s.

The modeling results demonstrate that SedFoam can capture the scour onset triggered by piping driven by a prescribed upstream–downstream pressure difference. The temporal evolution of this pressure difference and its relationship with the fine-scale bathymetric change around the pipe are very consistent with the laboratory observation described in Sumer et al. [1]. The present model results further provide insight into the seepage flow and the creeping movement of sediments during the piping process.

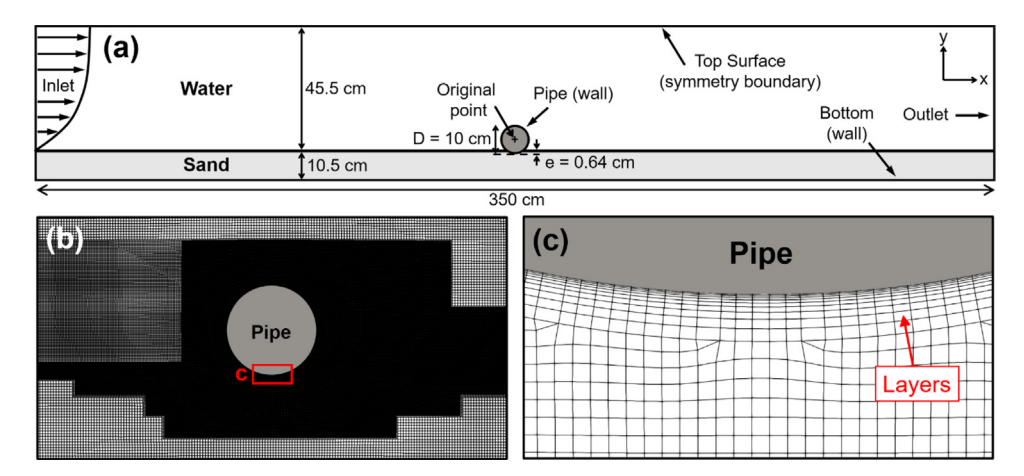


Fig. 4. (a) The sketch of the domain setup for simulating scour onset driven by a current, (b) the enlarged view of the mesh around the pipe, and (c) the zoom-in view of the mesh near the pipe surface at the bottom.

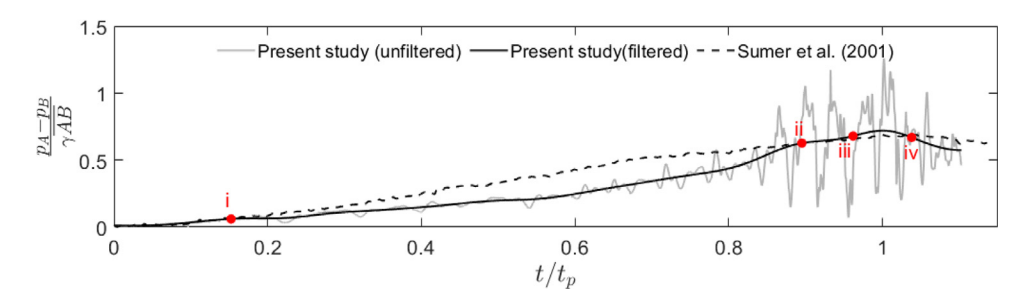
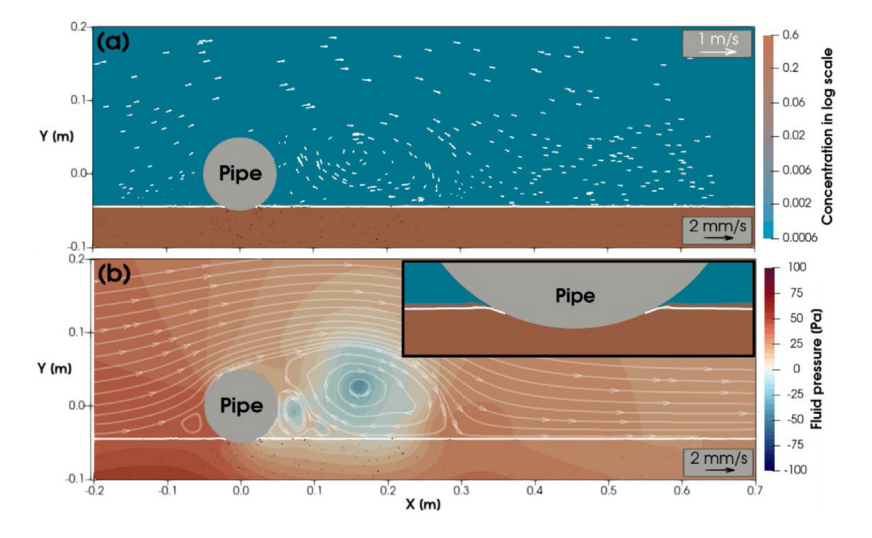


Fig. 5. The time series of the filtered and unfiltered fluid pressure gradient underneath the pipe between probe A and B driven by a unidirectional current for the model result (black and gray solid lines represent the filtered and unfiltered data), experimental data (black dash line). The four selected time instants (red dots) to be discussed in Figs. 6–9 are also indicated. The filtered pressure gradient time series from the model result is low-pass filtered at 0.1 Hz to remove the oscillation due to vortex shedding.



**Fig. 6.** A snapshot of the piping process driven by a unidirectional current at  $t/t_p = 0.15$  corresponding to the instant "i" denoted in Fig. 5. (a) Sediment concentration (contour), sediment bed (white line, sediment concentration equals  $\phi_f$ ), seepage velocity (black arrows), initial sediment bed (light brown line), and fluid velocity (white arrows). (b) Spatial distribution of fluid pressure (color contour), sediment bed (white line), seepage velocity (black arrows), and streamlines of the fluid velocity (gray lines). (For interpretation of the references to color in this figure legend, the reader is referred to the web version of this article.)

#### 3.2. Piping driven by a current

In the fluvial environment, flood-induced erosion and scour driven by intense currents is a leading factor causing infrastructure foundation damages. In the marine environment, currents can be one of the major hydrodynamic driving forces to cause scour, in addition, or in combination with wave motions. A two-dimensional model domain is set up to examine the scour onset

of a 2D pipeline driven by a unidirectional current. As shown in Fig. 4(a), the domain is a flume of 350 cm in length and 56 cm in depth with the lower 10.5 cm of the domain specified as the initial sediment bed. The model domain contains a circular pipe with diameter D=10 cm slightly buried in the sand bed with an initial burial depth of e=0.64 cm. The positive direction of x-axis is denoted as the current direction and the y-axis is defined as positive upward with x=0 and y=0

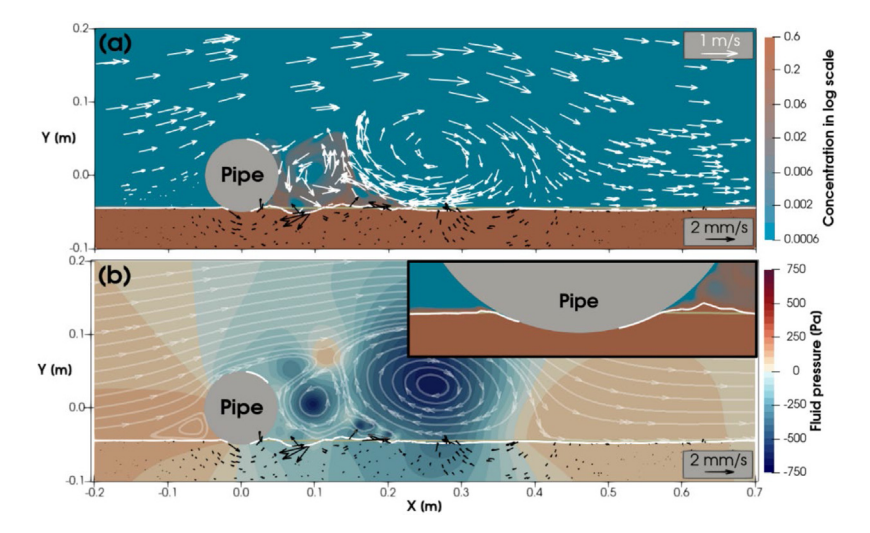


**Fig. 7.** A snapshot of the piping process driven by a unidirectional current at  $t/t_p = 0.90$  corresponding to the instant "ii" denoted in Fig. 5. (a) Sediment concentration (contour), sediment bed (white line, sediment concentration equals  $\phi_f$ ), seepage velocity (black arrows), initial sediment bed (light brown line), and fluid velocity (white arrows). (b) Spatial distribution of fluid pressure (color contour), sediment bed (white line), seepage velocity (black arrows), and streamlines of the fluid velocity (gray lines).. (For interpretation of the references to color in this figure legend, the reader is referred to the web version of this article.)

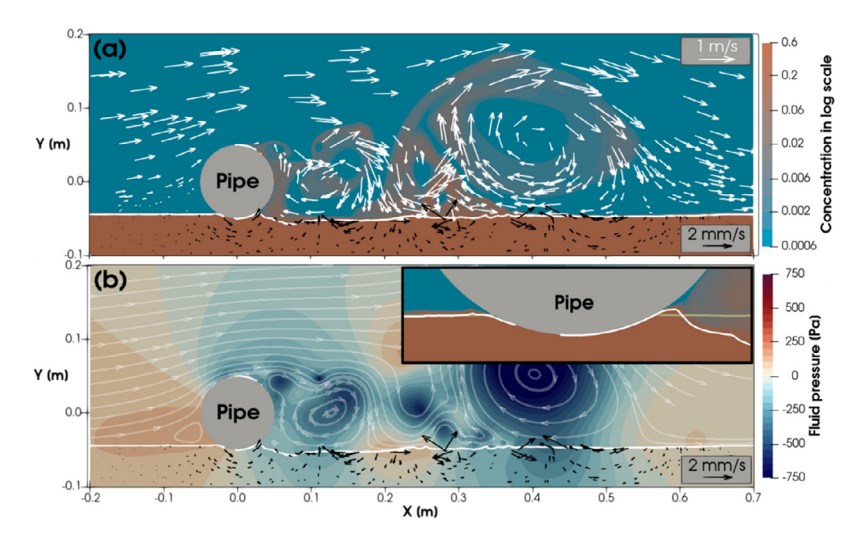


**Fig. 8.** A snapshot of the piping process driven by a unidirectional current at  $t/t_p = 0.96$  corresponding to the instant "iii" denoted in Fig. 5. (a) Sediment concentration (contour), sediment bed (white line, sediment concentration equals  $\phi_f$ ), seepage velocity (black arrows), initial sediment bed (light brown line), and fluid velocity (white arrows). (b) Spatial distribution of fluid pressure (color contour), sediment bed (white line), seepage velocity (black arrows), and streamlines of the fluid velocity (gray lines).. (For interpretation of the references to color in this figure legend, the reader is referred to the web version of this article.)

located at the center of the pipe. Two numerical probes used to record the upstream/downstream pressure difference are located at the same location as the prescribed pressure case discussed in Section 3.1 (see Fig. 1(a)). The boundary condition for the top domain boundary is a symmetry plane and the right boundary is specified as an outlet. The bottom boundary and the pipe surface are specified as wall boundary. In addition, wall functions for smooth walls are applied on the pipe surface for both k and  $\omega$ . A rough-wall logarithmic law velocity profile is applied at the inlet, which is written as

$$u_1^f = \frac{u_*}{\kappa} \ln \frac{30y}{K_s} \tag{19}$$

where  $\kappa=0.41$  is the von Karman constant,  $u_*$  is the friction velocity, and  $K_s$  is the roughness. Sumer et al. [1] carried out the unidirectional current experiment by increasing the current velocity gradually until the piping occurs. However, the time series of inlet flow velocity specified in the laboratory experiment was not provided. Here, we apply a similar incremental current with a prescribed roughness  $K_s=2.5d$  by adjusting the friction velocity

so that the piping occurs within a reasonable computational time. As presented in Fig. 4(b) The meshing strategy is similar to the previous case by first constructing a coarse stretch grid with 1.5 mm smallest squares. Then we refine the mesh around the bed and the pipe into a 0.375 mm mesh size. Different from the previous case, sublayers around the pipe are added to resolve the boundary layer around the pipe (see Fig. 4(c)). The total number of grid points is about 427 thousand. The simulation was carried out using 36 computing cores and it took 50 h (1800 CPU hours) for the entire 60-second run.

The comparison of the modeled and the measured upstream-downstream fluid pressure gradient (piezometric head gradient) between probe A and B is shown in Fig. 5. To make a fair comparison, the time series is normalized by  $t_p$ , defined as the time when the peak fluid pressure gradient occurs in the laboratory experiment ( $t_p = 88.5 \text{ s}$ ) and numerical simulation ( $t_p = 52.4 \text{ s}$ ). When the current passes the pipeline, vortex shedding occurs and these vortex motions cause wide range temporal fluctuations with a peak frequency at 0.57 Hz (see the gray line in Fig. 5).

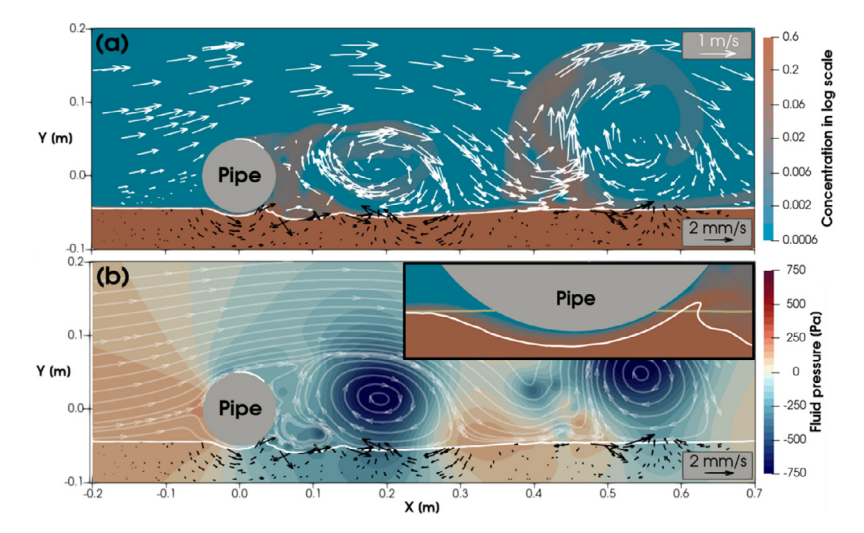


**Fig. 9.** A snapshot of the piping process driven by a unidirectional current at  $t/t_p = 1.04$  corresponding to the instant "iv" denoted in Fig. 5. (a) Sediment concentration (contour), sediment bed (white line, sediment concentration equals  $\phi_f$ ), seepage velocity (black arrows), initial sediment bed (light brown line), and fluid velocity (white arrows). (b) Spatial distribution of fluid pressure (color contour), sediment bed (white line), seepage velocity (black arrows), and streamlines of the fluid velocity (gray lines).. (For interpretation of the references to color in this figure legend, the reader is referred to the web version of this article.)

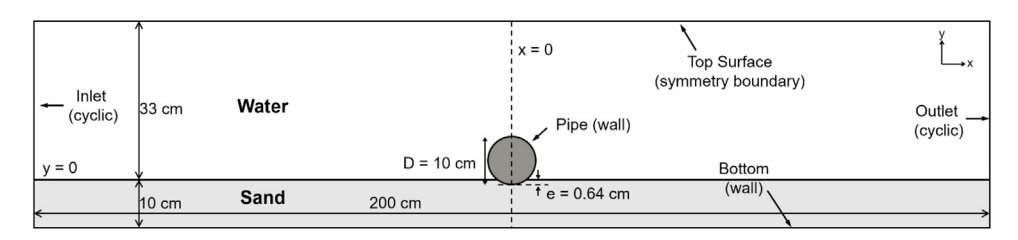


Fig. 10. The sketch of the domain setup for simulating scour onset driven by an oscillatory flow.

To compare with the measured data, the modeled pressure gradient time series is low-pass filtered at 0.1 Hz to remove the oscillations due to the vortices. A more in-depth discussion on these higher frequency vortex motions will be presented later. Here, we observe that the simulation captures the trend of the pressure gradient before and after the piping occurs. Unlike the prescribed pressure case studied in Section 3.1, in which the pressure gradient drops significantly right after the piping, the pressure gradient observed here drops to a certain extent but still maintains its magnitude after the piping because flow separation that causes the pressure gradient remains (see more discussion next). This feature is observed in the measured data and it is captured by the numerical model. However, the modeled pressure gradient oscillation and the peak value during piping are larger than the measured data. In addition to the uncertainties in the unidirectional flow forcing, the discrepancy can also be caused by the uncertainty in the preparation of the sediment bed between the laboratory experiment and numerical model, or due to the dilatancy effect.

Figs. 6–9 show more insight into the relationship between the flow field, seepage flow, and sediment transport during the piping process. As the ambient flow velocity around the pipe increases, the flow separates and a wake zone can be seen at the downstream side of the pipe (Fig. 6(a)). Even at this early stage of the flow separation, vortices are generated in the wake zone with the length roughly twice the pipe diameter. The flow structure in the wake zone essentially consists of a (clockwise) primary vortex and its returning flow further induces a (counterclockwise) secondary vortex. Simultaneously, a low-pressure wake region accompanied by the vortex-pair can be identified (see Fig. 6(b)). The center of the low-pressure region has a magnitude of -30 Pa and it is located at the core of the primary vortex (see x = 0.17

m). Away from the core, pressure increases but this low-pressure zone still has an effect that extends to the sediment bed where the pore pressure is closed to 0–30 Pa. On the other hand, due to the presence of the pipe, flow approaching the pipe decelerates significantly (see the nearly stagnant flow at around x=-0.05 m y=0 m). The fluid pressure just upstream of the pipe is about +50 Pa and the pore pressure in the bed is about the same level or slightly larger deeper into the bed. This upstream-downstream pore pressure gradient drives a weak seepage flow (below 0.1 mm/s) just beneath the pipe but it is not sufficient to trigger piping. Due to the proximity to the bed, the clockwise (primary) vortex is of higher intensity than the counterclockwise (secondary) vortex. It should be noted that the vortex pair start to move downstream at a later time,  $t/t_p=0.20$ , and forms a vortex street.

At a later time ( $t/t_p = 0.90$ ) when the ambient flow velocity approaching the pipe becomes larger, the vortex shedding pattern at the downstream of the pipe becomes more obvious (Fig. 7(a)). These vortices have caused some erosion and transport of sediments downstream of the pipe. A scour hole located downstream from the pipe at x = 0.07 m can be clearly seen. The scour hole is formed due to the action of the primary (clockwise) vortex eroding and transporting sediments upstream toward the pipe (not shown) and conversely due to the secondary (counterclockwise) vortex eroding and transporting sediment further downstream (see Fig. 7(a)). Importantly, the upstream-downstream pressure difference increases considerably both in the water column (about +150 Pa at upstream versus -300 Pa at downstream) and in the sediment bed (see Fig. 7(b)). At this moment, seepage velocity has built-up (see Fig. 7(b)) and reached a magnitude near 1-2 mm/s just beneath the pipe. Meanwhile, the gap between the pipe and the sediment bed at the downstream side begins to develop correspondingly (see the zoom-in plot of Fig. 7(b)) and the feature is similar to that shown in Fig. 3(a) for the prescribed pressure case. However, in this case, it is the presence of pipe obstructing the flow causing the large upstream-downstream pressure difference. When the flow velocity is sufficiently large, or when the pipe diameter is larger, more intense flow separation and significant upstream-downstream pressure gradient is expected.

The pressure difference slightly decreases before the breakthrough occurs (Fig. 8,  $t/t_p = 0.96$ ). Up to this moment, three vortices are observed downstream of the pipe and the vortex street pattern can be clearly identified. Moreover, the gap underneath the pipe has continued to grow (see inset in Fig. 8(b)). Although the pressure gradient slightly decreases, the seepage velocity still maintains a magnitude of 1-2 mm/s. A significant rise of sediment surface can be found on the downstream side of the pipe which is consistent with the experimental observation [1]. However, some of the sediment accumulation is due to the clockwise vortex delivering sediments from the downstream scour hole (at x = 0.08 m) to the upstream. Similar to the prescribed pressure case, the upstream side of the sediment bed is pushed toward the downstream direction and eventually the sediment bed breaches and the breakthrough occurs. As shown in Fig. 9, right after the breakthrough happens, a strong flow is ejected from the small gap beneath the pipe (see streamlines shown in Fig. 9(b)). Meanwhile, the sediments are eroded from this gap and transported downstream and the tunneling stage has begun.

Compared to the prescribed pressure case, the pore pressure difference, seepage flow, and the breaching/breakthrough processes are qualitatively similar to the present case driven by a unidirectional current. However, the source of the pressure difference in this case stems from the fluid mechanic response, namely, the presence of pipe decelerates the incoming flow and the wake behind the pipe. Moreover, vortices generated in the wake zone periodically erode and transport sediment upstream and downstream due to the vortex shedding and cause a small scour hole. However, this scour hole is located at about more than half a pipe diameter downstream and it does not directly affect the scour onset process. Our simulation demonstrates SedFoam's capability of capturing both fluid dynamic and piping processes simultaneously, and more importantly, the interaction between the two.

#### 4. Model application

In the previous section, the two-phase model SedFoam is used to simulate laboratory experiments reported by Sumer et al. [1] for the onset of scour, or called piping, of a slightly buried 2D fixed pipeline driven by a prescribed upstream-downstream pressure difference or by a unidirectional current. These two validations are very important because they demonstrate one of the main reasons to pursue a two-phase modeling methodology, that is, to allow more realistic interaction between flow, sediment transport, and seepage flow in response to the presence of structure. In this section, we further apply the two-phase model to simulate pipeline scour driven by an oscillatory flow with realistic scour onset and the subsequent scour process (Section 4.1) in order to generate a scour hole of sufficient size. Then, the pipeline is lowered artificially into the scour hole in order to test the model's capability to simulate the backfill process (Section 4.2).

#### 4.1. Pipeline scour driven by an oscillatory flow

We apply SedFoam to simulate scour onset and subsequent erosion driven by wave motions with a small initial burial depth. Sumer et al. [1] reported the scour onset of a pipeline driven by surface waves by carrying out a wave flume experiment. Because it is very computationally intensive to simulate both the local scour and the entire wave propagation and transformation in a wave flume, we simplify the problem by modeling pipeline scour similar to an oscillating water tunnel setup. As presented in Fig. 10, the pipeline is of diameter D = 10 cm and it is fixed over a sand bed of grain diameter d = 0.18 mm with a small initial burial depth of e = 0.64 cm (e/D = 0.064). These physical parameters are identical to those reported by Sumer et al. [1]. For the wave forcing, we drive the model with a sinusoidal oscillatory flow of wave period T = 4 s and velocity amplitude  $U_0 = 0.45$  m/s which takes about 4 wave periods to reach the targeted velocity amplitude (see Fig. 11(a)). It is important to point out that the oscillatory flow is assumed to be sinusoidal (symmetric between the positive and negative wave phase) in the model while in the laboratory flume experiment, the wave orbital velocity is positively-skewed due to nonlinear shallow-water waves [1]. Furthermore, surface waves can cause the boundary layer streaming effect and drive sediment transport in the direction of wave propagation [42,56]. Since SedFoam does not resolve the free surface, the boundary layer streaming effect is neglected in this study.

The model domain is of 200 cm in length and 43 cm in height with the lower 10 cm of the domain specified as the initial sediment bed. To reduce the computational domain length, the two lateral boundaries are specified as the cyclic boundary condition. To drive the oscillatory flow in such a periodic domain, a horizontal sinusoidal body force

$$f_1 = \rho^f \frac{\partial}{\partial t} \left( U_0 \sin \frac{2\pi t}{T} \right) \tag{20}$$

is specified in the *x*-momentum equation (see Eqs. (3) and (4)). The top domain boundary is specified as a symmetry plane while the bottom boundary is specified as a wall boundary. A base mesh of grid size 5 mm is used, and the mesh is locally refined to 1.25 mm near the pipe and the sediment bed. The simulation was carried out using 72 computing cores and it took 120 h (8640 CPU hours) for the entire 50-second run. Again, two numerical probes A and B used to record the upstream–downstream pressure difference are located at the same locations as those discussed in the previous sections. To facilitate the discussion later, during the wave crest (trough) interval, the wave-driven flow is directed to the right (left) and it is also referred to onshore (offshore) flow. Similarly, the left (right) side of the pipe is denoted as the offshore (onshore) side.

The time series of free-stream velocity and modeled pressure gradient (piezometric head gradient) calculated between probe A and probe B are shown in Fig. 11. The modeled pressure gradient underneath the pipeline increases during the first four waves subject to the increasing magnitude of free-stream velocity. In oscillatory flows, the free-stream pressure gradient is leading the free-stream velocity by 90 degrees (see Eq. (20)). Here, we observe that the pore pressure gradient underneath the pipe leads free stream velocity by about 54 degrees, suggesting that the model predicts an expected phase lag of local pore pressure gradient underneath the pipe relative to the free-stream horizontal pressure gradient by about 36 degrees. According to Sumer et al. [1], piping occurs when the horizontal (pore) pressure gradient in the bed exceeds the flotation (vertical) gradient:

$$\frac{\partial}{\partial x} \left( \frac{p^f}{\gamma} \right) \ge (1 - n) (s - 1) \tag{21}$$

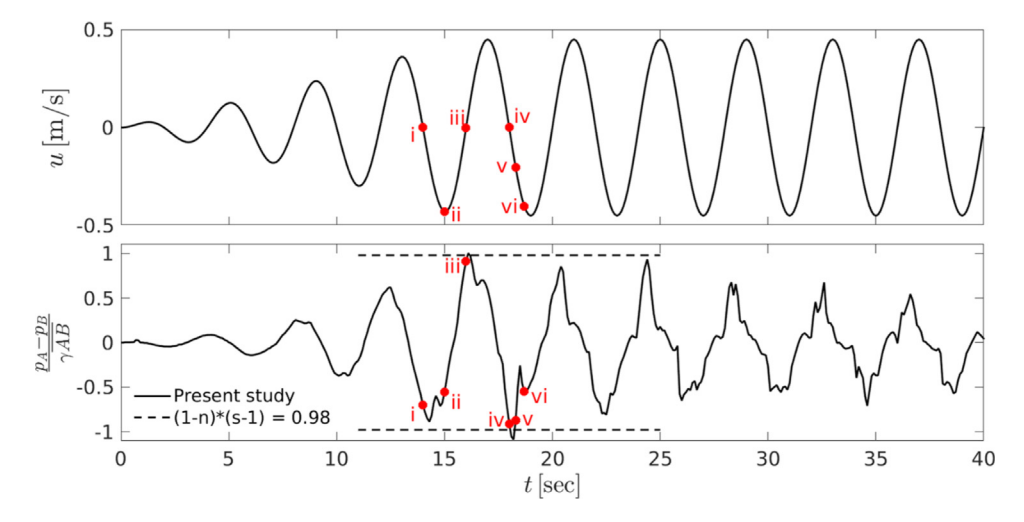
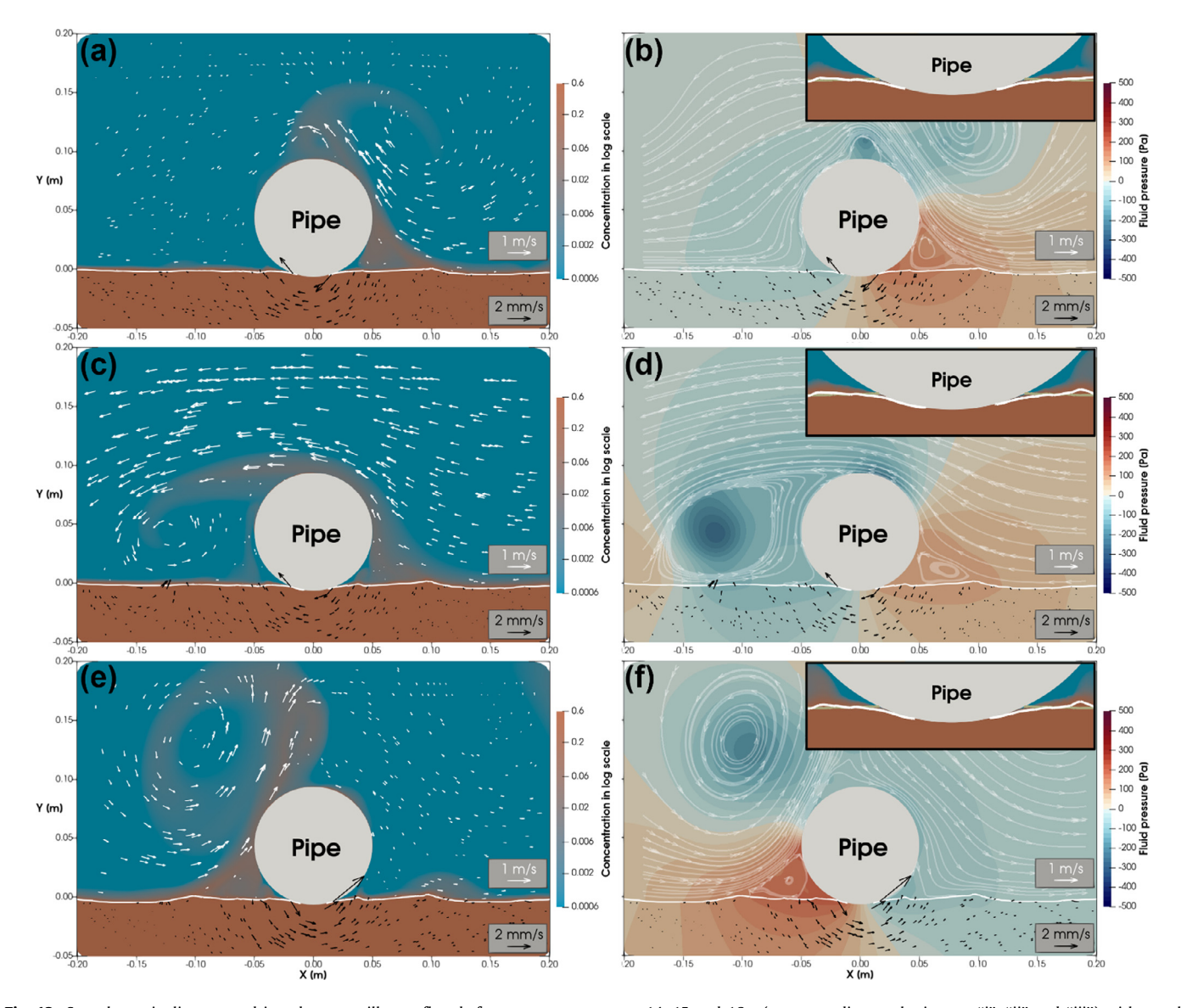
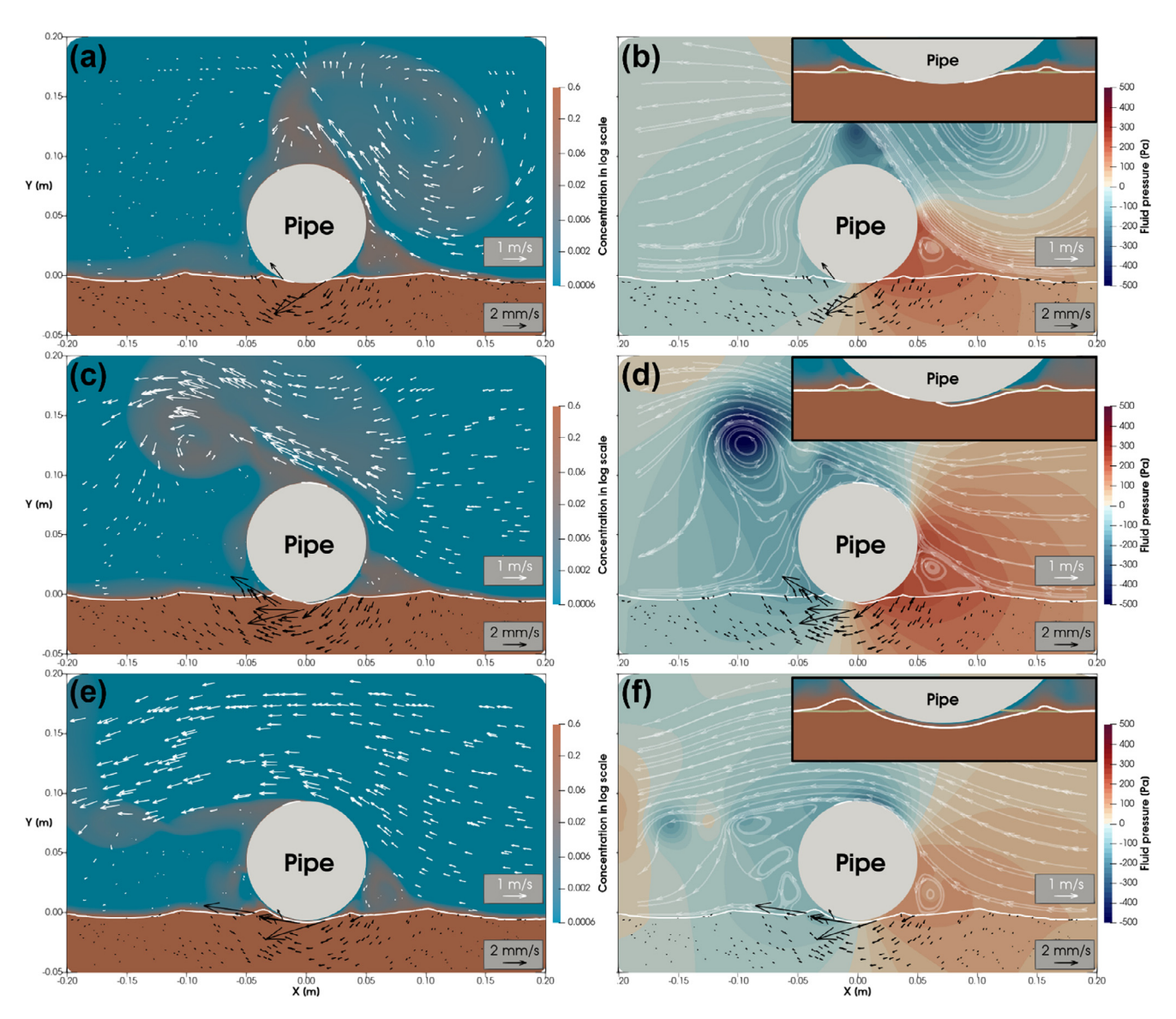


Fig. 11. The time series of (a) free-stream velocity and (b) pore pressure gradient underneath the pipe calculated between probe A and B (lower panel) with the dashed line represents the theoretical critical pressure gradient for piping. Red dots signified by i-vi are selected instants to be discussed in Figs. 12 and 13.



**Fig. 12.** Snapshots pipeline scour driven by an oscillatory flow before scour onset at t=14, 15 and 16 s (corresponding to the instant "i", "ii" and "iii") with panel (a), (c), and (e) show sediment concentration (color contour), sediment bed (white line, sediment concentration equals to  $\phi_f$ ), seepage velocity (black arrows), and fluid velocity (white arrows) and panel (b), (d) and (f) show fluid pressure (color contour), sediment bed (white line), seepage velocity (black arrows), and streamlines (gray lines).. (For interpretation of the references to color in this figure legend, the reader is referred to the web version of this article.)



**Fig. 13.** Snapshots pipeline scour driven by an oscillatory flow during scour onset at t=18, 18.3 and 18.7 s (corresponding to the instant "iv", "v" and "vi") with panel (a), (c), and (e) show sediment concentration (color contour), sediment bed (white line, sediment concentration equals to  $\phi_f$ ), seepage velocity (black arrows), and fluid velocity (white arrows) and panel (b), (d), and (f) show fluid pressure (color contour), sediment bed (white line), seepage velocity (black arrows), and streamlines (gray lines).. (For interpretation of the references to color in this figure legend, the reader is referred to the web version of this article.)

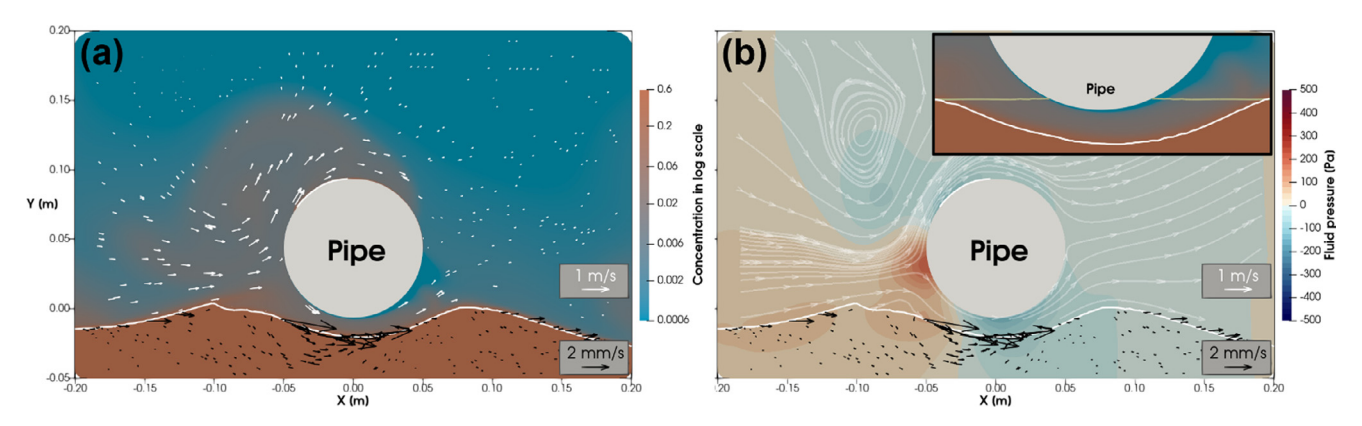


**Fig. 14.** Pipeline scour driven by an oscillatory flow at the end of the simulation (t=60~s) with (a) shows sediment concentration (color contour), sediment bed (white line, sediment concentration equals to  $\phi_f$ ), seepage velocity (black arrows), and fluid velocity (white arrows) and panel (b) shows fluid pressure (color contour), sediment bed (white line), seepage velocity (black arrows), and streamlines (gray lines).. (For interpretation of the references to color in this figure legend, the reader is referred to the web version of this article.)

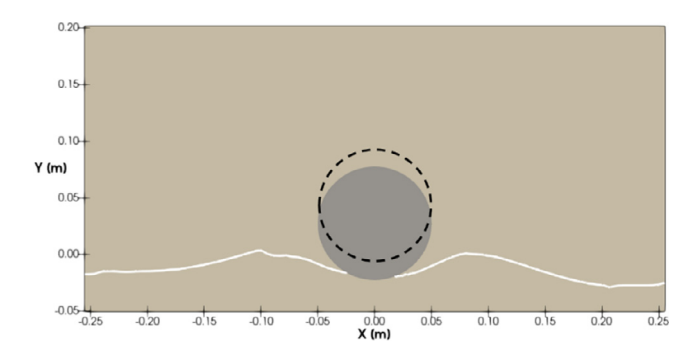


**Fig. 15.** Initial setup for the backfill simulation with the sediment bed represented by the thick white line with sediment concentration equals to  $\phi_f$ . The gray circle represents the pipeline which is artificially lowered from the previous scour simulation (dashed line).

where n is the porosity which can be calculated by the sediment concentration in the bed  $(n=1-\phi)$ . This criterion is called the (theoretical) critical value for piping in this study. Using s=2.717 and averaged sediment concentration in the bed as 0.57, the critical value is calculated to be 0.98. Under the crest of the  $5^{\rm th}$  wave, the pressure gradient underneath the pipe first exceeded the critical value for piping but only for a fraction of a second. As we will discuss next, the complete piping with breakthrough does not occur until the passage of wave trough of the  $5^{\rm th}$  waves. These important time points indicated in Fig. 11 will be discussed in detail next.

For the first few wave periods, some minor sediment suspensions occur away from the pipeline due to vortices in the wake zones. Close to the pipe, only very small changes of bathymetry (about 0.5 mm in the vertical direction) are observed while the seepage flow underneath the pipe is within 0.5 mm/s and there is no evidence of piping (not shown). During the trough interval of the 4th wave (t = 14-16 s), we start to see the development of a small gap between the cylinder and the sediment bed. At t = 14s near the onshore-offshore flow reversal (Fig. 12(a) and (b)), locally accelerated flow is already directed offshore and it was the remnant of the primary vortex generated from the previous wave crest interval. This offshore-directed flow impinges to the pipe and generates a sufficiently large offshore-directed pressure gradient to drive a seepage flow close to 1 mm/s underneath the pipe. One second later (t = 15 s, see Fig. 12(c) and (d)), this offshore-directed pressure gradient causes a small gap between the pipe and the sediment bed at the offshore side (see the inset of Fig. 12(d)). As shown in Section 3 (Fig. 3(a)), this instant signifies the beginning of the piping process. However, due to the short timescale of the wave period, the flow starts to reduce its intensity and the newly developed gap cannot continue to grow. One more second later at t = 16 s (see Fig. 12(e) and (f)) under the crest of the 5th wave, strong onshore-directed pressure gradient drives a seepage flow exceeding 1 mm/s, and a small gap is now observed at the onshore side of the pipe/sediment interface (see the inset of Fig. 12(f)). Thus, under the oscillatory flow, the gaps are growing from both sides as wave-induced flow changes its direction. According to the time series of pressure gradient shown in Fig. 11(b), the pressure gradient exceeds the theoretical critical value for a fraction of a second before the flow intensity reduces. Therefore, the piping process cannot continue and hence breakthrough of sediment bed underneath the pipe is not observed. The wave action during the trough of the 4th wave and the crest of the 5th wave, although cannot complete the piping process due to the short wave period, already leaves a notable gap between the pipe and the sediment bed at both sides.

At the onshore–offshore flow reversal in the 5<sup>th</sup> wave (t = 18 s, see Fig. 13(a) and (b)), we observe a more intense flow

passing over the pipe toward the offshore direction and stronger flow separation at the downstream side of the pipeline. At this moment, the pore pressure difference between the onshore and offshore side of the pipeline becomes much stronger (from about +150 to -150 Pa) than that of the 4<sup>th</sup> wave (compare with Fig. 12(b)), which drives larger seepage flow exceeding 2 mm/s underneath the pipeline. The gaps on both sides have grown significantly so that the remaining connected portion is relatively short (see the inset of Fig. 13(b)). The pore pressure gradient at this moment is near the critical value of piping (see Fig. 11(b)). Only 0.3 s later (t = 18.3 s, see Fig. 13(c) and (d)), we observe the beginning of breakthrough similar to those observed in the prescribed pressure case shown in Fig. 13(e) and (f). This small gap allows the incoming flow to enter the narrow space underneath the pipe where the offshore-directed flow breaches the sediment bed and expands the gap. A significant rise of the sediment bed can be observed on the offshore side (see the inset in Fig. 13(d)). Another 0.4 s later (see Fig. 13(e) and (f)), the piping process has been completed and the fixed pipeline is fully detached from the sediment bed. The small gap allows a high-speed flow to penetrate through and causes a more significant erosion. This instant also signifies the beginning of the tunnel erosion stage. By t = 60 s (Fig. 14), a 2 cm gap can be clearly seen between the pipe and the sediment bed. After the scour onset is completed, see Figs. 13(f) and 14(b), although the presence of the pipeline still induces a notable upstream-downstream pressure gradient, its magnitude becomes significantly smaller, particularly in the sediment bed. This can also be confirmed from the time series of the pressure difference between Probe A and B shown in Fig. 11 (b) after t = 18.3 s. Therefore, after the scour onset, the role of seepage flow on the overall scour development is of less importance. The KC number of this case is KC = 18. According to Sumer et al. [1] and Sumer and Fredsøe [11], the equilibrium scour depth is about 0.4D, which is 4 cm and it will take more than 10 min to reach the equilibrium scour depth. As the main focus of this paper is on the scour onset, further simulation to reach the equilibrium is not performed. In the next section, we will place the pipe into this 2 cm scour hole in order to test SedFoam's capability to model backfill.

#### 4.2. Backfill process

To simulate the backfill process, we use the sand bed obtained at t=60 s (Fig. 14) as the initial bathymetry. Furthermore, the pipeline is artificially lowered so that it is attached to the sediment bed and effectively sheltered by the adjacent sand bed by about 1/4 of the pipeline diameter (see Fig. 15). Consequently, the perturbations introduced by the pipeline and the bathymetry start to encourage backfill. Importantly, the artificial lowing method is an idealized treatment in this study to mimic self-burial process, which does not fully represent the realistic dynamic interactions between fluid, sediment and object movement. With the initial velocities of fluid and sediment phases specified as zero, we drive the model with the same oscillatory flow (sinusoidal oscillatory flow of wave period T=4 s and velocity amplitude of 0.45 m/s) but without the ramp-up stage.

As shown in Fig. 16(a) and (b), at the instant of offshore-onshore flow reversal, the primary vortex that has been generated in the previous wave trough interval reaches the local bathymetric hump located at x = -0.09 m. The vortex entrains and transports sediments toward the pipe and encourages more sediments to be accumulated near the pipe. One second later as the wave reaches the crest flow (Fig. 16(c) and (d)), the main flow is directed toward the onshore direction, and flow separation occurs at the onshore side of the pipe. The onshore-directed boundary layer flow again passes over the local hump while entrain and

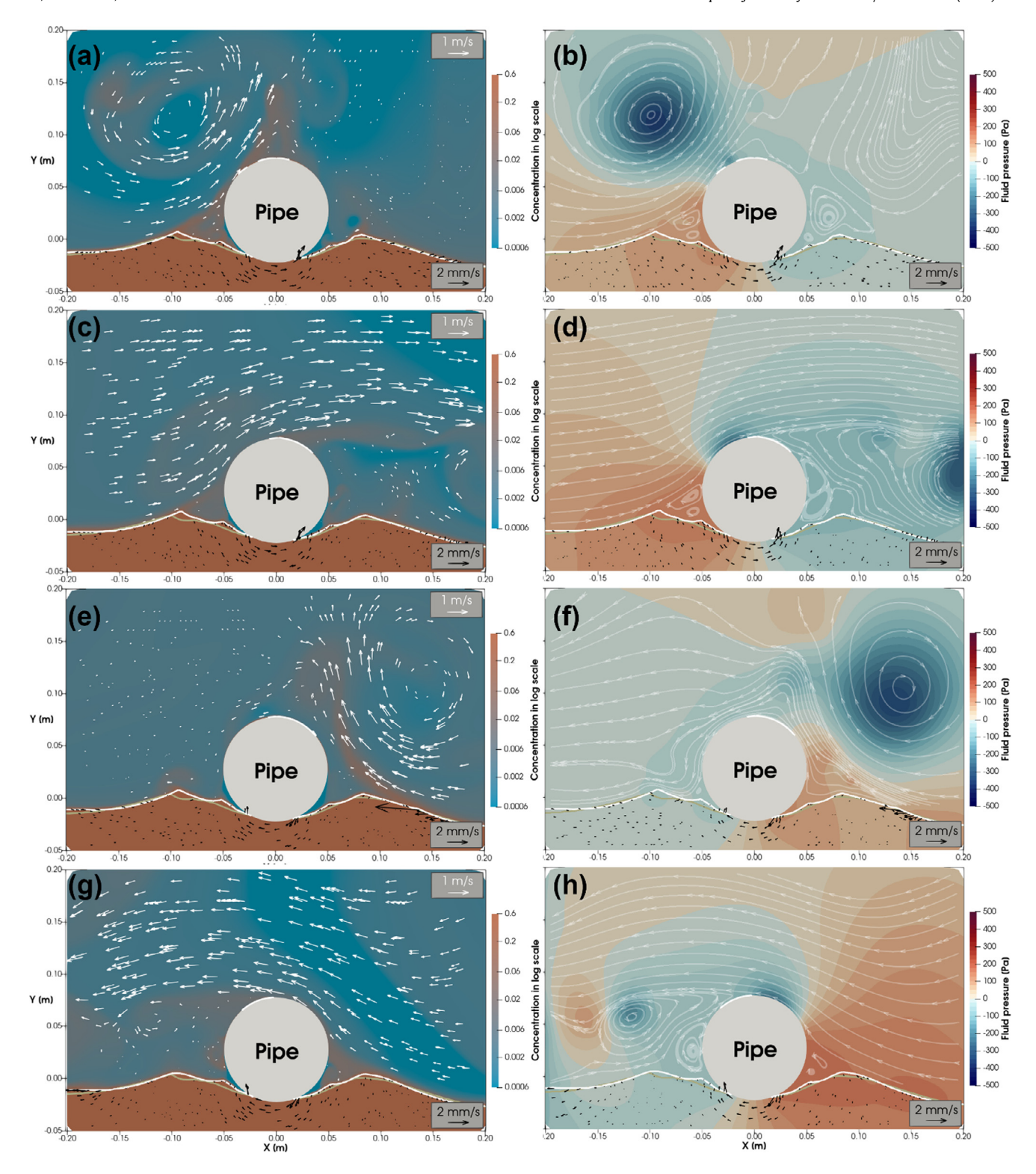


**Fig. 16.** Snapshots of sediment concentration and flow velocity (left panels) and dynamic pressure and streamlines (right panels) during the backfill process in the  $2^{\text{nd}}$  wave at offshore-onshore flow reversal (panel (a) & (b), t = 4 s), onshore flow peak (panel (c) & (d), t = 5 s), onshore-offshore flow reversal (panel (e) and (f), t = 6 s) and offshore flow peak (panel (g) and (h), t = 7 s). The fluid velocity and seepage velocity are represented by white and black arrows, respectively. The white line (light brown line) at the bottom represents the instantaneous (initial) sediment bed. (For interpretation of the references to color in this figure legend, the reader is referred to the web version of this article.)

deliver more sediments toward the pipe. At t=7 s of onshore-offshore flow reversal (Fig. 16(e) and (f)), the flow reverses and the primary vortex generated during the previous onshore flow interval is now ejected toward the pipe and meanwhile entrains and transports sediments from the onshore bathymetric hump

located at x = 0.08 m toward the pipe. While the offshore flow velocity magnitude keeps increasing, it continues to entrain and deliver more sediments from the onshore hump toward the pipe while a new vortex is being generated at the offshore side of the pipe (Fig. 16(g) and (h)). It is worth pointing out that the fluid

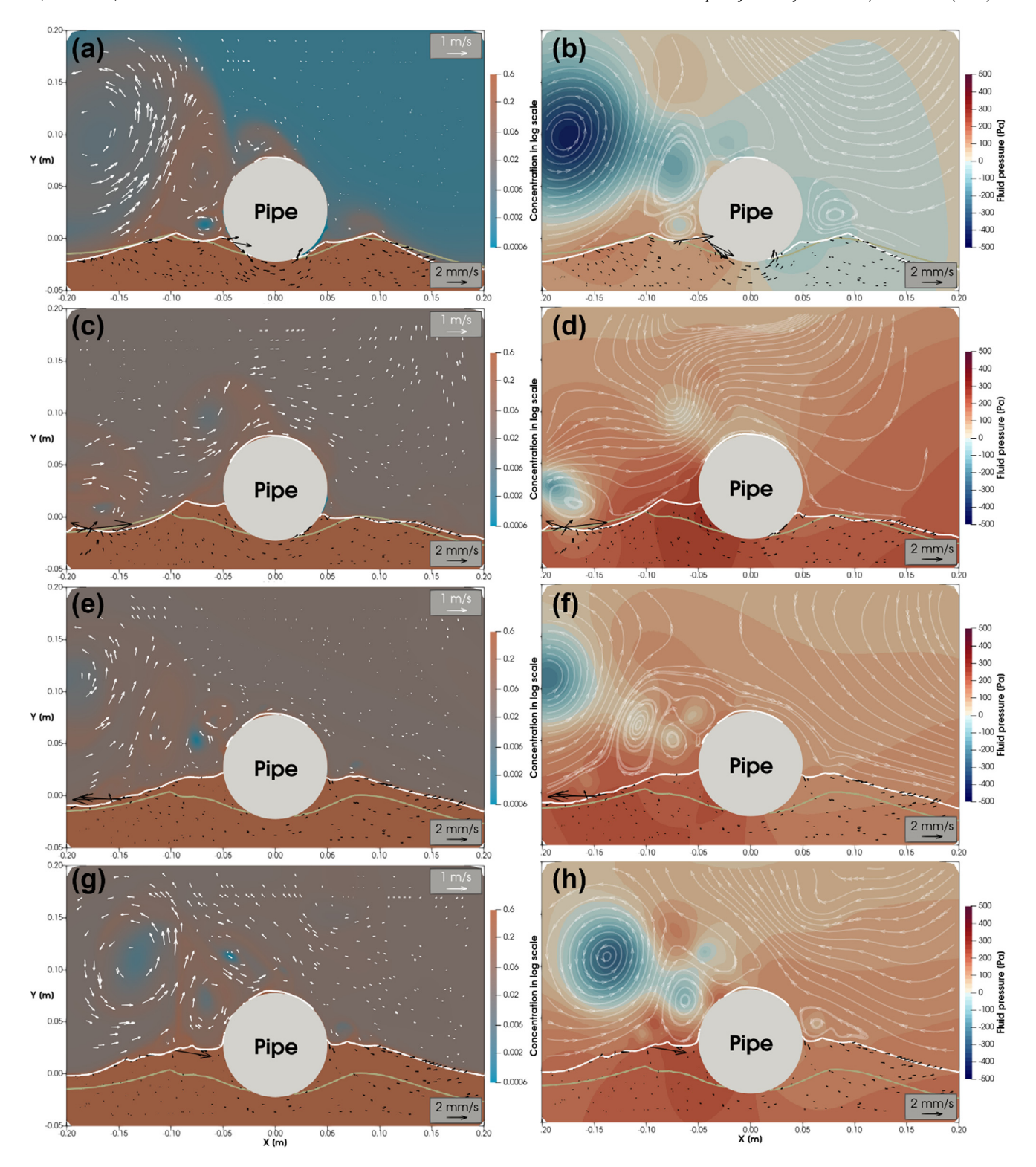


**Fig. 17.** Snapshots of sediment concentration and flow velocity (left panels) and dynamic pressure and streamlines (right panels) during the backfill process at the  $3^{rd}$  wave (panel (a) & (b), t = 12 s), the 6th wave (panel (c) & (d), t = 24 s), the 9th wave (panel (e) & (f), t = 36 s) and the 12th wave (panel (g) & (h), t = 48 s). The fluid velocity and seepage velocity are represented by white and black arrows, respectively. The white line (light brown line) at the bottom represents the instantaneous (initial) sediment bed. (For interpretation of the references to color in this figure legend, the reader is referred to the web version of this article.)

pressure difference due to the presence of the pipe still exists, yet its effect is less influential than the sediment transport driven by the vortices. Clearly, the local bathymetric features interact with the vortices and encourage sediment transport toward the pipe and causing backfill. Similar cycles continue and eventually causing significant burial of the pipe.

Fig. 17 shows the backfill/burial process at the end of every three wave-cycles. After the action of three wave-periods, the small spaces between the sediment bed and pipe have been filled up (see Fig. 17(a) and (b), compare the instantaneous bathymetry represented by the white line with the initial bathymetry represented by the light-brown line). After six wave periods (Fig. 17(c)

and (d)), the sediments around the pipe begin to pile up although the bed level at the offshore side is higher. In the following instant at the ninth wave (Fig. 17(e) and (f)), the onshore side of the bed level increases significantly and the backfill at both sides of the pipe is of a similar level. Subsequent backfill become more balanced at both sides of the pipe (Fig. 17(g) and (h)) and the sediments keep on accumulating and end up reach about half of the pipe diameter. According to the empirical formula provided by Sumer et al. [1], at KC = 18, the burial depth (similar to scour depth) is 0.4D, which is similar to the present model results. By examining the pressure distribution at different stages of the backfill process (see Fig. 17(b), (d), (f) and (h)), it is important to point out that at the beginning of the backfill, the presence of pipeline cause larger offshore-onshore pressure gradient. However, toward the end of the backfill, the pressure distribution is much more uniform and the pressure gradient becomes very small. SedFoam model results presented here confirm the intuitive idea that the sediment backfill process is driven by balancing the protrusion of the object and recovering the pressure field back to a more uniform distribution.

#### 5. Conclusions

An Eulerian two-phase numerical modeling framework for sediment transport applications, SedFoam, has been applied to simulate the scour onset via piping process and backfill process. The model is validated with a laboratory experiment reported by Sumer et al. [1] for the onset of scour of a slightly buried 2D fixed pipeline driven by a prescribed pressure difference between two sides of the pipe. The model is able to reproduce the observed piping, including the formation of a small gap and rise of sand at the downstream side, the subsequent expansion of the gap to the upstream side, and the final breaching underneath the pipe triggered by the larger seepage velocity. The corresponding upstream-downstream pressure gradient evolution beneath the pipe is also in agreement with measure data. When further applying the model to simulate scour onset via piping driven by a unidirectional current, the model can simulate the increase of upstream-downstream pressure difference caused by the fluid dynamic processes due to flow separation and the local piping process.

As the most existing scour CFD models do not directly resolve piping as the scour onset, we apply SedFoam, as a first proof-of-concept attempt, to simulate scour hole development underneath a pipeline with a small initial burial depth driven by an oscillatory flow at Keulegan–Carpenter number KC=18 although the streaming effect is not considered here. The model's capability of simulating the burial processes has also been demonstrated by artificially placing the pipeline in a shallow trench and the simulated final burial depth is similar to that predicted by the empirical formula. Future work should focus on implementing the capability of moving object following the force balance law and the equation of motion in order to carry out full simulations of scour and burial of pipeline.

The model investigation presented in this paper demonstrate a key advantage of a two-phase modeling methodology, that is, to allow the simulation of more realistic interactions between the hydrodynamics, the presence of structure, soil response, and sediment transport. However, to more accurately model soil response, future model extension is necessary. For example, it is widely recognized that the concentration region of sediments shows the behaviors of fluid-like and solid-like transition due to the dilatancy effect as sediment concentration is below or above the critical concentration [57]. For wet soil considered here, the dilatancy effect is directly coupled with the pore-pressure response due to microstructure rearrangement of the soil skeleton,

which reinforces the fluid or solid behaviors. The consideration of small amount of air is also an import issue which directly causes damping and phase lag of pore pressure change. These important mechanisms should be incorporated into the Eulerian two-phase models to expand the model applicability for a wider range of applications involving sediment transport, seepage flow, and soil responses.

#### **Declaration of competing interest**

The authors declare that they have no known competing financial interests or personal relationships that could have appeared to influence the work reported in this paper.

#### Acknowledgment

This research is supported by Strategic Environmental Research and Development Program, United States (MR20-1478) and NSF, United States (OCE-1756714). J. Chauchat and A. Mathieu would also like to acknowledge the financial support from Agence de l'Innovation de Défense (AID), Shom through project MEPELS and Agence Nationale de la Recherche (ANR) through project SheetFlow (ANR-18-CE01-0003). Numerical simulations presented in this study were carried out using the Caviness cluster at University of Delaware, and the Stampede2 cluster at the University of Texas at Austin via XSEDE. Part of the computations presented in this paper were also performed using the GENCI infrastructure under Allocations A0060107567 and A0080107567 and the GRICAD infrastructure. We are grateful to the developers involved in OpenFOAM, who lay the foundation of the SedFoam model.

#### References

- [1] B.M. Sumer, C. Truelsen, T. Sichmann, J. Fredsøe, Onset of scour below pipelines and self-burial, Coast. Eng. 42 (2001) 313–335, http://dx.doi.org/ 10.1016/S0378-3839(00)00066-1.
- [2] S.I. Voropayev, F.Y. Testik, H.J.S. Fernando, D.L. Boyer, Burial and scour around short cylinder under progressive shoaling waves, Ocean Eng. 30 (2003) 1647–1667, http://dx.doi.org/10.1016/S0029-8018(02)00146-4.
- [3] S.T. Demir, M.H. García, Experimental studies on burial of finite-length cylinders under oscillatory flow, J. Waterw. Port Coast. Ocean Eng. 133 (2007) 117–124, http://dx.doi.org/10.1061/(ASCE)0733-950X(2007) 133:2(117).
- [4] F.Y. Testik, S.I. Voropayev, H.J.S. Fernando, S. Balasubramanian, Mine burial in the shoaling zone: Scaling of laboratory results to oceanic situations, IEEE J. Ocean. Eng. 32 (2007) 204–213, http://dx.doi.org/10.1109/JOE.2007. 890970
- [5] M. Mattioli, A. Mancinelli, M. Brocchini, Experimental investigation of the wave-induced flow around a surface-touching cylinder, J. Fluids Struct. 37 (2013) 62–87, http://dx.doi.org/10.1016/j.jfluidstructs.2012.10.002.
- [6] S.E. Rennie, A. Brandt, C.T. Friedrichs, Initiation of motion and scour burial of objects underwater, Ocean Eng. 131 (2017) 282–294, http://dx.doi.org/ 10.1016/j.oceaneng.2016.12.029.
- [7] R. Whitehouse, Scour at Marine Structures: A Manual for Practical Applications, Thomas Telford Ltd, 1998, http://dx.doi.org/10.1680/sams. 26551.
- [8] C.T. Friedrichs, S.E. Rennie, A. Brandt, Self-burial of objects on sandy beds by scour: A synthesis of observations, in: J. Harris, R. Whitehouse, S. Moxon (Eds.), Scour Eros., CRC Press, 2016, pp. 179–189, http://dx.doi.org/10.1201/ 9781315375045.
- [9] A.A. Németh, S.J.M.H Hulscher, H.J. DeVriend, Modelling sand wave migration in shallow shelf seas, in: Cont. Shelf Res., Pergamon, 2002, pp. 2795–2806, http://dx.doi.org/10.1016/S0278-4343(02)00127-9.
- [10] P. Traykovski, T. Austin, Continuous Monitoring of Mobility, Burial and Re-Exposure of Underwater Munitions in Energetic Near-Shore Environments, SERDP Project MR-2319 Final Report, 2017, https://www.serdp-estcp.org/ Program-Areas/Munitions-Response/Munitions-Underwater/MR-2319 (accessed September4, 2020).
- [11] B.M. Sumer, J. Fredsøe, The Mechanics of Scour in the Marine Environment, World Scientific, 2002, http://dx.doi.org/10.1142/4942.
- [12] Y. Mao, The interaction between a pipeline and an erodible bed, 1986.

- [13] Y.M. Chiew, Mechanics of local scour around submarine pipelines, J. Hydraul. Eng. 116 (1990) 515–529, http://dx.doi.org/10.1061/(ASCE)0733-9429(1990)116:4(515).
- [14] Y. Li, M.C. Ong, D.R. Fuhrman, CFD investigations of scour beneath a submarine pipeline with the effect of upward seepage, Coast. Eng. 156 (2020) 103624, http://dx.doi.org/10.1016/j.coastaleng.2019.103624.
- [15] M. Mattioli, J.M. Alsina, A. Mancinelli, M. Miozzi, M. Brocchini, Experimental investigation of the nearbed dynamics around a submarine pipeline laying on different types of seabed: The interaction between turbulent structures and particles, Adv. Water Resour. 48 (2012) 31–46, http://dx.doi.org/10.1016/j.advwatres.2012.04.010.
- [16] C.K.K. Lun, S.B. Savage, D.J. Jeffrey, N. Chepurniy, Kinetic theories for granular flow: Inelastic particles in Couette flow and slightly inelastic particles in a general flowfield, J. Fluid Mech. 140 (1984) 223–256, http: //dx.doi.org/10.1017/S0022112084000586.
- [17] F. Boyer, É. Guazzelli, O. Pouliquen, Unifying suspension and granular rheology, Phys. Rev. Lett. 107 (2011) 188301, http://dx.doi.org/10.1103/ PhysRevLett.107.188301.
- [18] J.T. Jenkins, D. Berzi, Dense inclined flows of inelastic spheres: Tests of an extension of kinetic theory, in: Granul. Matter, Springer, 2010, pp. 151–158, http://dx.doi.org/10.1007/s10035-010-0169-8.
- [19] C.E. Ozdemir, T.J. Hsu, S. Balachandar, A numerical investigation of fine particle laden flow in an oscillatory channel: The role of particle-induced density stratification, J. Fluid Mech. 665 (2010) 1–45, http://dx.doi.org/10. 1017/S0022112010003769.
- [20] M.I. Cantero, S. Balachandar, A. Cantelli, C. Pirmez, G. Parker, Turbidity current with a roof: Direct numerical simulation of self-stratified turbulent channel flow driven by suspended sediment, J. Geophys. Res. Ocean 114 (2009) C03008, http://dx.doi.org/10.1029/2008JC004978.
- [21] M.M. Nasr-Azadani, E. Meiburg, Turbidity currents interacting with threedimensional seafloor topography, J. Fluid Mech. 745 (2014) 409–443, http://dx.doi.org/10.1017/jfm.2014.47.
- [22] V. Marieu, P. Bonneton, D.L. Foster, F. Ardhuin, Modeling of vortex ripple morphodynamics, J. Geophys. Res. Ocean 113 (2008) C09007, http://dx.doi. org/10.1029/2007JC004659.
- [23] Y.J. Chou, O.B. Fringer, A model for the simulation of coupled flow-bed form evolution in turbulent flows, J. Geophys. Res. Ocean 115 (2010) C10041, http://dx.doi.org/10.1029/2010|C006103.
- [24] A. Khosronejad, F. Sotiropoulos, Numerical simulation of sand waves in a turbulent open channel flow, J. Fluid Mech. 753 (2014) 150–216, http://dx.doi.org/10.1017/jfm.2014.335.
- [25] C. Baykal, B.M. Sumer, D.R. Fuhrman, N.G. Jacobsen, J. Fredsoe, Numerical investigation of flow and scour around a vertical circular cylinder, Philos. Trans. R. Soc. A Math. Phys. Eng. Sci. 373 (2015) 20140104, http://dx.doi. org/10.1098/rsta.2014.0104.
- [26] D. Liang, L. Cheng, Numerical model for wave-induced scour below a submarine pipeline, J. Waterw. Port Coast. Ocean Eng. 131 (2005) 193–202, http://dx.doi.org/10.1061/(ASCE)0733-950X(2005)131:5(193).
- [27] D.R. Fuhrman, C. Baykal, B. Mutlu Sumer, N.G. Jacobsen, J. Fredsøe, Numerical simulation of wave-induced scour and backfilling processes beneath submarine pipelines, Coast. Eng. 94 (2014) 10–22, http://dx.doi. org/10.1016/j.coastaleng.2014.08.009.
- [28] X. Liu, M.H. García, Three-dimensional numerical model with free water surface and mesh deformation for local sediment scour, J. Waterw. Port Coast. Ocean Eng. 134 (2008) 203–217, http://dx.doi.org/10.1061/(ASCE) 0733-950X(2008)134:4(203).
- [29] D. Zeidan, E. Romenski, A. Slaouti, E.F. Toro, Numerical study of wave propagation in compressible two-phase flow, Int. J. Numer. Methods Fluids 54 (2007) 393–417, http://dx.doi.org/10.1002/fld.1404.
- [30] G. Ma, F. Shi, J.T. Kirby, A polydisperse two-fluid model for surf zone bubble simulation, J. Geophys. Res. 116 (2011) 5010, http://dx.doi.org/10. 1029/2010jc006667.
- [31] E. Goncalves, D. Zeidan, Simulation of compressible two-phase flows using a void ratio transport equation, Commun. Comput. Phys. 24 (2018) http://dx.doi.org/10.4208/cicp.oa-2017-0024.
- [32] J. Ding, D. Gidaspow, A bubbling fluidization model using kinetic theory of granular flow, AIChE J. 36 (1990) 523–538, http://dx.doi.org/10.1002/aic. 690360404.
- [33] D. Zeidan, R. Touma, A. Slaouti, Application of a thermodynamically compatible two-phase flow model to the high-resolution simulations of compressible gas-magma flow, Internat. J. Numer. Methods Fluids 76 (2014) 312–330. http://dx.doi.org/10.1002/fld.3936.
- [34] J.R. Finn, M. Li, S.V. Apte, Particle based modelling and simulation of natural sand dynamics in the wave bottom boundary layer, J. Fluid Mech. 796 (2016) 340–385, http://dx.doi.org/10.1017/jfm.2016.246.
- [35] S.K. Jha, F.A. Bombardelli, Toward two-phase flow modeling of nondilute sediment transport in open channels, J. Geophys. Res. Earth Surf. 115 (2010) http://dx.doi.org/10.1029/2009JF001347.

- [36] Z. Cheng, T.J. Hsu, J. Calantoni, SedFoam: A multi-dimensional Eulerian two-phase model for sediment transport and its application to momentary bed failure, Coast. Eng. 119 (2017) 32–50, http://dx.doi.org/10.1016/j. coastaleng.2016.08.007.
- [37] J. Chauchat, Z. Cheng, T. Nagel, C. Bonamy, T.J. Hsu, SedFoam-2.0: A 3-D two-phase flow numerical model for sediment transport, Geosci. Model Dev. 10 (2017) 4367–4392, http://dx.doi.org/10.5194/gmd-10-4367-2017.
- [38] M. Ouda, E.A. Toorman, Development of a new multiphase sediment transport model for free surface flows, Int. J. Multiph. Flow 117 (2019) 81–102, http://dx.doi.org/10.1016/j.ijmultiphaseflow.2019.04.023.
- [39] P. Dong, K. Zhang, Intense near-bed sediment motions in waves and currents, Coast. Eng. 45 (2002) 75–87, http://dx.doi.org/10.1016/S0378-3839(02)00040-6.
- [40] A. de J.Kozakevicius, D. Zeidan, A.A. Schmidt, S. Jakobsson, Solving a mixture model of two-phase flow with velocity non-equilibrium using WENO wavelet methods, Internat. J. Numer. Methods Heat Fluid Flow 28 (2018) 2052–2071, http://dx.doi.org/10.1108/HFF-05-2017-0215.
- [41] Z. Cheng, J. Chauchat, T.J. Hsu, J. Calantoni, Eddy interaction model for turbulent suspension in Reynolds-averaged Euler-Lagrange simulations of steady sheet flow, Adv. Water Resour. 111 (2018) 435–451, http://dx.doi. org/10.1016/j.advwatres.2017.11.019.
- [42] Y. Kim, Z. Cheng, T.J. Hsu, J. Chauchat, A numerical study of sheet flow under monochromatic nonbreaking waves using a free surface resolving Eulerian two-phase flow model, J. Geophys. Res. Ocean 123 (2018) 4693–4719, http://dx.doi.org/10.1029/2018JC013930.
- [43] Y. Kim, R.S. Mieras, Z. Cheng, D. Anderson, T.J. Hsu, J.A. Puleo, D. Cox, A numerical study of sheet flow driven by velocity and acceleration skewed near-breaking waves on a sandbar using SedWaveFoam, Coast. Eng. 152 (2019) 103526, http://dx.doi.org/10.1016/j.coastaleng.2019.103526.
- [44] A. Mathieu, J. Chauchat, C. Bonamy, T. Nagel, Two-phase flow simulation of tunnel and lee-wake erosion of scour below a submarine pipeline, Water 11 (2019) 1727, http://dx.doi.org/10.3390/w11081727.
- [45] T. Nagel, J. Chauchat, C. Bonamy, X. Liu, Z. Cheng, T.J. Hsu, Three-dimensional scour simulations with a two-phase flow model, Adv. Water Resour. 138 (2020) 103544, http://dx.doi.org/10.1016/j.advwatres.2020. 103544.
- [46] A. Salimi-Tarazouj, T.J. Hsu, P. Traykovski, Z. Cheng, J. Chauchat, A numerical study of onshore ripple migration using a Eulerian two-phase model, J. Geophys. Res. Ocean 126 (2021) http://dx.doi.org/10.1029/2020[C016773.
- [47] M.H. Kazeminezhad, A. Yeganeh-Bakhtiary, A. Etemad-Shahidi, J.H. Baas, Two-phase simulation of wave-induced tunnel scour beneath marine pipelines, J. Hydraul. Eng. 138 (2012) 517–529, http://dx.doi.org/10.1061/ (ASCE)HY.1943-7900.0000540.
- [48] C.H. Lee, Y.M. Low, Y.M. Chiew, Multi-dimensional rheology-based twophase model for sediment transport and applications to sheet flow and pipeline scour, Phys. Fluids 28 (2016) 053305, http://dx.doi.org/10.1063/1. 4948987.
- [49] G. MiDi, On dense granular flows, Eur. Phys. J. E 14 (2004) 341–365, http://dx.doi.org/10.1140/epje/i2003-10153-0.
- [50] D.A. Drew, Mathematical modeling of two-phase flow, Annu. Rev. Fluid Mech. 15 (1983) 261–291, http://dx.doi.org/10.1146/annurev.fl.15.010183. 001401
- [51] D.C. Wilcox, Turbulence Modeling for CFD, third ed., DCW Industries, San Diego, California, 2006.
- [52] Y. Forterre, O. Pouliquen, Flows of dense granular media, Annu. Rev. Fluid Mech. 40 (2008) 1–24, http://dx.doi.org/10.1146/annurev.fluid.40.111406. 102142.
- [53] J. Chauchat, M. Médale, A three-dimensional numerical model for incompressible two-phase flow of a granular bed submitted to a laminar shearing flow, Comput. Methods Appl. Mech. Engrg. 199 (2010) 439–449, http://dx.doi.org/10.1016/j.cma.2009.07.007.
- [54] P.C. Johnson, R. Jackson, Frictional-collisional constitutive relations for granular materials, with application to plane shearing, J. Fluid Mech. 176 (1987) 67–93, http://dx.doi.org/10.1017/S0022112087000570.
- [55] J. Chauchat, A comprehensive two-phase flow model for unidirectional sheet-flows, J. Hydraul. Res. 56 (2018) 15–28, http://dx.doi.org/10.1080/ 00221686.2017.1289260.
- [56] P. Blondeaux, G. Vittori, A. Bruschi, F. Lalli, V. Pesarino, Steady streaming and sediment transport at the bottom of sea waves, J. Fluid Mech. 697 (2012) 115–149, http://dx.doi.org/10.1017/jfm.2012.50.
- [57] M. Pailha, M. Nicolas, O. Pouliquen, Initiation of underwater granular avalanches: Influence of the initial volume fraction, Phys. Fluids 20 (2008) 111701, http://dx.doi.org/10.1063/1.3013896.